

80701

NACA TN 4364

0067170



TECH LIBRARY KAFB, NM

NATIONAL ADVISORY COMMITTEE FOR AERONAUTICS

TECHNICAL NOTE 4364

AN INVESTIGATION OF SUPERSONIC TURBULENT BOUNDARY
LAYERS ON SLENDER BODIES OF REVOLUTION IN FREE
FLIGHT BY USE OF A MACH-ZEHNDER INTER-
FEROMETER AND SHADOWGRAPHS

By Alvin Seiff and Barbara J. Short

Ames Aeronautical Laboratory
Moffett Field, Calif.



Washington

September 1958

APR 10 1959
TECHNICAL LIBRARY
AF 2011



0067170

TECHNICAL NOTE 4364

AN INVESTIGATION OF SUPERSONIC TURBULENT BOUNDARY

LAYERS ON SLENDER BODIES OF REVOLUTION IN FREE

FLIGHT BY USE OF A MACH-ZEHNDER INTER-

FEROMETER AND SHADOWGRAPHS

By Alvin Seiff and Barbara J. Short

SUMMARY

Slender bodies of revolution in free flight at Mach numbers of 3.2 and 3.6 were photographed in a Mach-Zehnder interferometer and the pictures were analyzed to obtain the turbulent-boundary-layer density distributions for the case of a body surface cold compared to recovery temperature. The density distributions obtained, when averaged, were found to be similar to those given by a theoretical equation of Crocco for a wide range of assumed velocity profiles. The average heat-transfer coefficients of the boundary layers also were obtained by an energy balance computation from the measured density distributions and measurements of the boundary-layer thickness, with the assumption that the velocity profile could be represented by a power law. The heat-transfer rates obtained could be adequately predicted by the T' method for estimating skin friction together with the modified Reynolds analogy.

The interference fringes from the interferometer and the instantaneous density distributions obtained from them indicate the presence of large scale local fluctuations in air density in the boundary layer. The magnitude of the fluctuations was a large fraction of the total variation of density in the mean density profiles. Corresponding to these density fluctuations, patterns could be seen in shadowgraph pictures of the boundary layers consisting of spot images in one of several successive arrangements. At low Reynolds numbers, the spots were comparable in size to the boundary-layer thickness and were arranged in single-file order along the surface. At higher Reynolds numbers (above 7 million in one case) the spots began to appear two in depth. Another picture of very highly developed turbulence showed the spots present six in depth and arranged in backward slanting rows. It is suggested that these spots are shadowgraph images of individual eddies, and the various arrangements cited indicate several stages of development of the turbulent boundary layer.

INTRODUCTION

The use of an optical interferometer as an instrument for the study of boundary layers was suggested as early as 1940 by Zobel, reference 1. However, the experimental difficulties inherent in the instrument have discouraged its use. It is difficult to construct, difficult to align, difficult to provide with a point light source which is sufficiently monochromatic and bright, difficult to insulate from the effects of vibration and noise, and the photographs obtained are difficult to interpret. It should be emphasized that none of these difficulties is insurmountable, but ordinarily it has been easier to survey boundary layers with pitot probes and total temperature probes than it has been to use the interferometer. One application of the interferometer to a boundary-layer problem is reported by Blue, reference 2. He surveyed a supersonic laminar boundary layer on a flat plate. Perhaps the predominant finding of Blue was that the light refraction effects were so severe as to require first-order corrections on the data which he obtained.

Counterbalancing the above difficulties are certain advantages associated with the use of an interferometer for boundary-layer surveys. It provides a way of surveying the flow without introducing any source of flow disturbance, which is a principal objection to the use of probes. Also, the usual limitation due to probe size is avoided. If equipped with a short-duration light source, the interferometer will give the instantaneous distribution of density, not subject to lag or time-averaging effects inherent in some other instruments. The most significant advantage for present purposes, however, was that the interferometer could be used to survey the boundary layers on gun-launched models in flight, a result that could not be accomplished in any more conventional way.

Initially, the objective of these experiments was to measure the heat transfer from a supersonic turbulent boundary layer to a bounding wall which was cold compared to the recovery temperature, since this was the relation of wall temperature to recovery temperature expected to occur most often in supersonic flight. This kind of boundary layer could be established by gun-launching a suitable model at supersonic speed through still air at room temperature, as was noted in references 3 and 4. To provide information on the heat transfer, it appeared that the optical interferometer might in this case be particularly appropriate.

It was a further objective to study the density profiles in supersonic turbulent boundary layers on both a time average and an instantaneous basis. The time average profile of temperature, which is generally taken to be inversely proportional to the time average profile of density, has been related to the time average profile of velocity by Crocco, reference 5. His equation has been used many times in theoretical treatments of the turbulent boundary layer and in experimental investigations also, to provide average profiles of temperature and density. The Crocco relation has been checked experimentally in references 6 and 7 by use of total temperature probe and pitot-probe measurements. It was an objective of

the present investigation to evaluate the Crocco equation further by use of average density profiles determined from the interferometer.

The instantaneous profiles of density in a turbulent boundary layer have remained relatively unknown. The only source of experimental information on the density fluctuations has been the hot wire anemometer, and this instrument responds to fluctuations in density, velocity, and temperature, separately or in combination, and the effects of these variables are not easy to separate. Furthermore, at supersonic speeds where the temperature and density variations become large and therefore of heightened interest, the hot wire becomes limited by frequency response. Therefore, present knowledge of the density fluctuations in supersonic turbulent boundary layers is very limited.

Interest in such fluctuations probably derives mostly from a broader interest in the structure of the turbulent boundary layer. From measurements of the fluctuations, deductions as to the scale and arrangement of the turbulence might reasonably be expected. The structure of turbulent flows has preoccupied many investigators, but no really satisfactory picture has yet emerged. Generally, turbulence is considered to be random and statistical which may be a way of saying that it contains no recognizable or recurrent patterns of structure. It was an objective of this test, therefore, to utilize the instantaneous character of the measurements to look for patterns of structure in the density profiles. Since shadowgraph pictures also are responsive to density variations (second derivative), free use was also made of instantaneous shadowgraphs of the models in flight, to supplement the use of the interferograms for this purpose.

The tests were conducted at Mach numbers of 3.2 and 3.6 and at length Reynolds numbers from 10 to 25 million. Brief descriptions of this work have been given earlier in references 8 and 9.

SYMBOLS

a, b, i, μ	dimensionless coefficients and zone numbers in data reduction equation
c	speed of light in air at density ρ , ft/sec
c_0	speed of light in vacuum, ft/sec
C_f	local skin-friction coefficient, dimensionless
C_F	mean skin-friction coefficient, dimensionless
c_p	heat capacity at constant pressure, Btu/slug $^{\circ}\text{R}$
d	body diameter, ft

\bar{h}	mean heat-transfer coefficient, Btu/sec ft ² °R
I	momentum loss integral defined by equation (17), dimensionless
J	mechanical equivalent of heat, ft lb/Btu
k	Gladstone-Dale constant, ft ³ /slug
l	length, ft
n	exponent in velocity profile equation, dimensionless
Pr	Prandtl number, dimensionless
q	heat-transfer rate, Btu/sec ft ²
r	radial coordinate from model axis, ft
R	Reynolds number, dimensionless
S	fringe shift, dimensionless
\overline{St}	mean Stanton number, dimensionless, based on boundary-layer-edge conditions
t	time, sec
T	temperature, °R
u	velocity, ft/sec
x	coordinate along body axis or along body surface, ft
y	coordinate normal to body surface, ft
z	coordinate along light ray direction, ft
δ	boundary-layer thickness, ft
λ	wave length of light, ft
ρ	air density, slugs/ft ³
θ	boundary-layer momentum thickness, ft
Φ	cone half-angle, deg

Subscripts

1	identifies air properties at boundary-layer edge
∞	identifies air properties in undisturbed free stream
e	edge of axially symmetric density field
r	recovery or adiabatic wall value
sh	at shock wave
S	air properties at a stagnation point on the model
w	wall or body surface

EXPERIMENTS

It was necessary to design models with boundary layers thick enough for accurate measurement. Usual small-scale projectiles, of the order of 3 inches long, have turbulent-boundary-layer thicknesses of the order of 0.020 to 0.030 inch. From inspection of preliminary interferograms, it was evident that these were inadequate for accurate survey. Since the boundary-layer thickness depends primarily on model length, long models were designed which could still be gun-launched at high speed without structural failure. Two types that were developed are indicated by sketches in figure 1.

Models

The first models tested were 6-inch-long fin-stabilized ogive-cylinders. They were launched without spin from a caliber 50 Mann barrel by use of the sabot and powder case indicated in figure 2(a). To obtain high strength-weight ratio for withstanding the launching loads, the models were machined from aluminum alloy, 7075-T. One of the ogive-cylinders used herein was in reality a cone-cylinder with the corner well rounded (see fig. 1). For the purposes of the present report, this nose is considered equivalent to the ogival nose used on the other models.

Later tests were made with 12-inch-long slender cones. These were likewise made of 7075-T aluminum alloy and were aerodynamically stabilized by use of a thin-skirt construction from the station $x/l = 0.3$ to the base. This placed the center of gravity at 0.64l and was accomplished by machining, starting with a solid cone, to leave a thin-walled shell 0.040 inch thick. As a matter of interest, the final weight of the models

was about one-sixth of the weight of the solid cone. The wall thickness and hole depth were selected on the basis of strength for withstanding launching loads as well as for aerodynamic stability.

The sabot for launching this model is indicated in figure 2(b). It consisted of an aluminum cap on a nylon tube. The model was held onto the sabot by evacuating the interior of the model through a small hole in the aluminum cap which was sealed by a piece of electrical tape serving as a check valve. In the gun, powder pressure bursts the tape, builds up inside the model, and acts to separate the model from the sabot when they emerge from the gun. A 1.75-inch smooth-bore gun 70 calibers long was employed in this case.

The models were polished by a procedure found, in reference 3, to give a surface with roughness amplitude generally less than 10 microinches, and maximum amplitude of the order of 25 microinches. This maximum corresponds to about 0.0004 of the boundary-layer thickness in the survey region, or about 1 percent of the laminar sublayer thickness. It is therefore believed that the test results should be representative of smooth surfaces:

Boundary-layer trips were applied to the model tips in the first 1/4 inch of length by sandblasting with No. 80 carborundum grit. This produced small craters with upset edges. Figure 3 is a photomicrograph at 100X of the roughened region of the first ogive-cylinder. Rough projections up to 0.0017 inch occur on this model. Similar pictures of other models showed maximum roughness as small as 0.0006 inch. These trips were effective in causing almost immediate transition to turbulence, as shown by the shadowgraphs of figure 4.

Test Conditions

The models were tested in still air at atmospheric pressure and room temperature in the test section of the Ames supersonic free-flight wind tunnel, reference 10. The interferometer was located between shadowgraph stations 3 and 4. Shadowgraph sequences of the flight through the test section were recorded for use in flow visualization and measurement of velocity, angle of attack, and boundary-layer thickness. The test conditions for the five rounds described in this paper are tabulated below.

Model number	Type	Mach number	Length Reynolds number, million	Angle of attack, deg	Station
1	Ogive-cylinder	3.15	10.5	0.5	Interferometer
2	Ogive-cylinder	3.21	10.8	.5	Interferometer
3	Ogive-cylinder	3.2	11	.3	Shadowgraph No. 4 top
4	Cone	3.64	24.8	1.2	Interferometer
5	Cone	3.45	22.8	.6	Shadowgraph No. 2 side

The Interferometer

The Mach-Zehnder interferometer used, developed by J. F. Darsow of the Ames Laboratory instrument research group, is a very large interferometer. The splitter plates are 13 inches in diameter and the field of view with the splitter plates inclined 45° is approximately 9 by 13 inches. The mirrors are mounted in a rigid Invar frame, illustrated in the photograph of figure 5, and are alined by electrically driven cams remotely controlled from the camera station. The principles of operation and construction of Mach-Zehnder interferometers generally similar to this one have been extensively discussed in the literature (see, e.g., refs. 1, 11, and 12).

The principal limitation of this interferometer and other similar interferometers is the light source which should ideally be a monochromatic point source. For the present application, submicrosecond duration was also required to effectively "stop" the models in flight, and the short duration led to a requirement of very great light intensity to give adequate photographic exposure. The light source selected on the basis of these requirements was a spark between magnesium electrodes, followed by an optical filter to pass the green triplet lines (wave lengths of 5167, 5173, and 5184 Å) in the magnesium spectrum. The spark was provided by discharge of a half microfarad condenser at 23 kilovolts, which gave very great intensity. The duration was measured electrically from voltage fluctuations across the spark gap and found to be about 3 microseconds. The source dimensions at the entrance slit were 0.3 inch high by 0.1 inch wide. Two different optical filters were used at different times during the test period: one was a monochromator consisting of an ethyl cinnamate (liquid filled) prism and associated lenses; and the other was an interference filter. The monochromator had a band pass width of about 235 Å centered around 5170 Å while the interference filter had a band pass width of 150 Å (at 90 percent cut off) according to the curve supplied by the

manufacturer. However, pictures of the spectral distribution of light from the spark obtained through the monochromator showed that in this region of the spectrum the only lines present were the triplet lines desired, and the background of continuum radiation was of relatively low intensity (perhaps one-tenth to one-fourth as bright as the lines). From this, it might be expected that the two filters would give comparable results, and this was the experience obtained.

In spite of the deviations from an ideal source, pictures of acceptable quality were obtained. Three of the best are shown in figure 6 along with an enlargement of one. These pictures were made at a magnification of about one-fourth to increase the intensity of light on the film and give adequate photographic exposure. The fringes are oriented normal to the body surface to give a continuous profile of density in the boundary layer. The diminishing contrast of the fringes near the sides of the pictures is due to the deviations from an ideal light source.

REDUCTION OF DATA

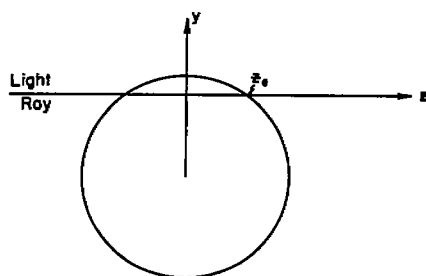
Analysis of the Interferograms

The Mach-Zehnder interferometer is fundamentally a device for detecting minute changes in the speed of light which result from changes in the density of the air medium through which the light is passed. The light velocity is related to the air density by the relation

$$c_0/c = 1 + kp \quad (1)$$

where c_0 is the velocity in vacuum and k is the Gladstone-Dale constant, which depends somewhat on the frequency of the light and has the value of $0.1168 \text{ ft}^3/\text{slug}$ for a wavelength of 5170 \AA . Thus, the light speed through air at normal atmospheric density differs from that through vacuum according to the ratio, $1/1.00028$.

The time required for a light ray to traverse a path of length $2z_e$ through an axially symmetric density disturbance is given by



$$t = 2 \int_0^{z_e} \frac{dz}{c} \quad (2)$$

(for cases where refraction can be neglected).
A ray in the undisturbed free stream will in the same time travel the distance

$$c_\infty t = 2 \int_0^{z_e} \frac{c_\infty}{c} dz \quad (3)$$

The portion of the wave front which passes through the disturbed flow will then lag behind the wave front which has passed through the free stream by some number of wavelengths, S (which may be positive or negative)

$$S\lambda = 2 \int_0^{z_e} \left(\frac{c_\infty}{c} - 1 \right) dz \quad (4)$$

and this phase difference will, at recombination with the reference beam, result in a fringe shift, S , when compared to the fringe pattern for the undisturbed free stream. By use of equation (1), equation (4) is converted to an expression for the fringe shift in terms of a density integral,

$$S = \frac{2k}{\lambda} \int_0^{z_e} (\rho - \rho_\infty) dz \quad (5)$$

Equation (5) may readily be used, for axially symmetric flow, to compute fringe shifts from a given density distribution, and may somewhat less readily be used to compute the density distribution from a given set of fringe shift data.

To find the density distribution from fringe shift data, the approximation attributed in reference 11 to C. C. van Voorhis is employed. The axially symmetric flow cross section is divided into a large number of annular zones, and the density is assumed to vary linearly with radius in each zone; that is, the curve of density variation is approximated by a large number of straight line segments. Evaluation of the density begins at the outermost zone. The density at the outer boundary of the disturbance is known, but the slope dp/dr within the zone is unknown and is computed from the fringe shift recorded at the inner boundary of the zone. This defines the outer zone. The next ray, tangent to the inner boundary of the second zone, crosses two zones of which the outer one is known. Therefore, its fringe shift is used to define dp/dr in the second zone. This process is carried out repeatedly to define the entire flow. The procedure is described in detail in reference 11, where the series equation,

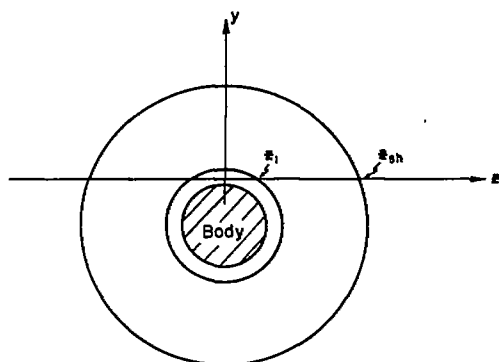
$$\frac{S_1 \lambda}{wk} = a_{1,i}(\rho_1 - \rho_\infty) + \sum_{\mu=i+1}^N b_{1,\mu}(\rho_\mu - \rho_\infty) \quad (6)$$

is developed to replace equation (5). Here, w is the uniform radial zone width, a and b are geometric coefficients depending on the relative length of the ray path within the zone, and i and μ are zone boundary numbers. The coefficients a and b have been tabulated in reference 11 for a 50-zone division of the flow cross section, from the axis to the shock wave.

To divide a cross section of the flow field, from the axis to the shock wave, into the 50 zones provided for in van Voorhis' tables would result in only two or three zones within the boundary layer and would give a very poor approximation to the boundary-layer density profile. Although van Voorhis' method provides for a subdivision of zones, an auxiliary table of coefficients must be made with the aid of the master table. The master table, however, does not include enough indices to draw up the auxiliary table necessary for the present investigation; that is, the master table must be extended before the auxiliary table can be made.

Fortunately, however, one can treat the boundary-layer region of the disturbed flow field as a separate disturbance superimposed upon the general flow disturbance. This can be shown by expressing the fringe shift integral of a ray which passes through the boundary layer as the sum of two integrals, one for the boundary layer and one for the external flow.

$$S = \frac{2k}{\lambda} \int_0^{z_1} (\rho - \rho_\infty) dz + \frac{2k}{\lambda} \int_{z_1}^{z_{sh}} (\rho - \rho_\infty) dz \quad (7)$$



In a similar way, the hypothetical fringe shift, S' , which would be developed by this ray if there were no boundary layer but, instead, a region with the density constant at the boundary-layer-edge value, ρ_1 , may be written,

$$S' = \frac{2k}{\lambda} \int_0^{z_1} (\rho_1 - \rho_\infty) dz + \frac{2k}{\lambda} \int_{z_1}^{z_{sh}} (\rho - \rho_\infty) dz \quad (8)$$

Now the difference, $S - S'$, is the additional fringe shift due to the boundary layer; that is, it is the difference between the fringe shift observed and that which would be measured if the boundary-layer region were filled by air at the constant density, ρ_1 .

$$\Delta S = S - S' = \frac{2k}{\lambda} \int_0^{z_1} (\rho - \rho_1) dz \quad (9)$$

Thus we obtain an equation of the same form as equation (5) with ρ_∞ replaced by ρ_1 and S replaced by ΔS .

Now, a smooth extrapolation to the surface of the fringes in the flow field external to the boundary layer would be expected to correspond to a smooth extension of the inviscid density distribution to the surface. That is, such a fringe curve should correspond to the inviscid density distribution. In the case of the ogive-cylinder, the density distribution

in the inviscid flow near the surface was found to be constant within the accuracy obtained from reduction of complete interferograms. Therefore, fringe shifts in the boundary layer measured to the extrapolated boundary-layer-edge fringe as base line should correspond precisely to the ΔS of equation (9). In the case of the cone, the inviscid density distribution is not exactly constant near the surface, but in the region occupied by the boundary layer, undergoes a variation of only 0.4 of a percent. Therefore the assumption that the inviscid fringe corresponds to the condition of constant density would appear valid and, again, ΔS is measured from an extrapolation of the fringe external to the boundary layer.

This method of analysis increased the number of zones into which the boundary layer could readily be divided, and therefore increased the accuracy obtained. It also greatly reduced the labor of data reduction.

Measurement of Fringes

The fringe coordinates were measured with a device called a coordinate comparator which translates a reading microscope over the field of view of the photograph in two mutually perpendicular directions. The position of the microscope parallel to the body surface, the x coordinate, is determined by and read from an accurate lead screw. The position normal to the body surface, the y coordinate, was set by a rack and pinion gear arrangement and read from a dial gage. The microscope position was read with an accuracy of 0.0001 inch in both directions, which is of the order of 0.5 percent of the boundary-layer thickness and 0.2 to 0.4 percent of the fringe spacing at the scale of the original photographic negatives. This does not insure, however, that the errors of reading will be this small, as judgment is required to place the microscope cross hair on the center of the fringe. To aid in this setting, microscope magnifications of from 4X to 14X were employed, depending on the film grain and fringe contrast. The repeatability of individual settings was generally within one or two thousandths of an inch or within about 4 percent of the fringe spacing. A set of fringe data from the cone is given in figure 7. The fringes of this figure are the ones numbered 1 through 6 in the interferogram of figure 6(c). The degree of accuracy of the measurements can be deduced from the scatter in the data, particularly near the edge and outside the boundary layer. A smooth line fairing of the fringes in this area does not miss any single reading point by more than 0.002 inch and the root-mean-square deviation would plainly be less than 0.001 inch, or 2 percent of the fringe spacing.

The most interesting characteristic of these fringes is their irregularity, which can be seen also in the photographic prints of figures 6(c) and 6(d). Pronounced irregularities did not appear in the pictures of the ogive-cylinder, although on some fringes, discontinuities in slope and curvature can be seen and detailed differences in slope and shape of adjacent fringes occurred rather generally.

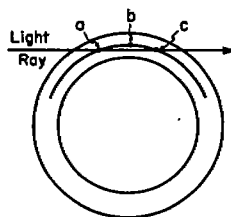
Figure 7 illustrates the technique of finding the additional fringe shift due to the boundary layer. The fringes in the free stream are extrapolated linearly to the surface, and this line is taken to be the base line or line of zero fringe shift for analysis of the boundary layer, as was discussed in the preceding section.

For reduction of the data, the variation of the fringe shift with y at constant x is required. In the case of the ogive-cylinders, it was simply assumed that the variation of S with y along the fringe would not differ significantly from the variation of S with y at constant x . This assumption was believed to have produced little error in the final results for these models. For the cone, however, this assumption was no longer tenable because the fringe contours obtained in this way were sometimes multiple-valued functions (as may be seen in fig. 7), giving rise to the physically impossible result of multiple values of density at a given point. Actually, the meaning of the multiple-valued fringe curves was that the density sometimes changed very rapidly with x as well as with y . This is shown by the cross plot of figure 7 which is given in figure 8. By reading fringe shifts at constant x from figure 8, single-valued fringe-shift curves were obtained.

Accuracy

In addition to errors of measurement of the fringe shifts, discussed above, possible causes of error include deviation from axial symmetry and refraction error. Angle of attack causes a departure from axial symmetry. Precautions were taken to obtain small angles of attack at the interferometer station and, consequently, resultant angles of attack were limited to 0.5° and 1.2° (see tabulation of test conditions). The effect of these small angles of attack on the results was evaluated by comparing the boundary-layer thickness and the density profiles obtained on opposite sides of the body. Comparison of the boundary-layer thicknesses showed that the asymmetry in thickness was small, although measurable in the case of the cone at 1.2° . The density distributions, however, showed no systematic difference between windward and sheltered sides, and it is considered that the angles of attack were small enough to have caused no serious inaccuracy in results.

Another cause of asymmetry lies in the turbulence itself. Because of the nature of turbulence, we might expect the density to vary at points a , b , and c in the sketch. For example, an eddy core may occur at b , but not at a and c . In fact, it is possible for the entire range of densities corresponding to the particular level y above the surface to occur along the arc a , b , c , in which case axial symmetry will not exist. The effect of this deviation from axial symmetry is very complex and difficult to analyze, particularly in the absence of specific information on the detailed variations in density to be expected along the arc. Intuitively, it might



be expected that the density profiles obtained would be intermediate between instantaneous profiles in a plane and average profiles. No single light ray averages conditions along the arc but, in the analysis by zones, the density at the edge of each inside zone depends on all the outer zones, and through this connection the averaging process can occur. In the averaging, special weight is given to the region near the vertical plane of symmetry because, in this region, the length of light path within the zone is relatively long. For the same reason, the interferometer is most sensitive to the density distribution in the vertical plane of symmetry. Hence, it appears that the density distributions obtained should be viewed as limited spatial averages with heavy weighting on the density profiles near the vertical plane of symmetry. It is believed that the profiles obtained by assuming axial symmetry lie intermediate between instantaneous profiles in a plane and average profiles.

Refraction errors, which were predominant in reference 2, have been calculated and found to be negligible for the present conditions. The deviation of the light ray in the boundary layer from its ideal straight path is proportional to the square of the ray path length which ranged from 0.2 to 0.8 inch in the present tests, about an order of magnitude shorter than in reference 2. In the worst case, it was calculated that the ray path departed by 0.0005 inch from a straight path in the boundary layer. Since this is less than 0.5 percent of δ , it resulted in a negligible error in the fringe shift due to deviation from the idealized straight path. A second kind of refraction error, intersection of the light ray on the film at the wrong location relative to the model surface, was minimized by having the interferometer camera in focus on the plane of flight. For errors in the plane of focus of as much as 3 inches, the location error on the film was computed to be within the reading accuracy.

The errors in measurement of free-stream density were of the order of 1 percent or less. Therefore, except for the lack of axial symmetry due to turbulence discussed above, it appears that there was no source of systematic error present, and the over-all error was that due to reading fringes. From comparison of repeat reductions, the disagreement was found to be of the order of 10 percent (see example cited under Results and Discussion). Hence, this is believed to be the order of accuracy of the density data.

RESULTS AND DISCUSSION

The density profiles from the ogive-cylinder tests are given in figure 9. From model 1, figure 9(a), the results of analyzing six fringes selected at random from the region of best fringe contrast are shown. The angle of attack in the plane of the picture was less than 0.1° , but in the other plane it was 0.5° . Therefore, the data are representative of the sides of a body at small angle of attack. In the case of model 2, figure 9(b), the resultant angle of attack was again 0.5° with a component in the plane of the picture of 0.4° so that the profiles are representative

of windward and sheltered side boundary layers. Three of the fringes are from the windward side and three are from the sheltered side. No systematic difference was evident.

The results of two independent readings and reductions of data are shown for the station $x = 5.4$ inches on the sheltered side of model 2. (Compare the filled circles with the open circles.) The difference between the two is about one-third the total scatter of the data.

The y coordinate in this figure has been made dimensionless relative to the boundary-layer thickness, measured from the interferograms and the shadowgraph of model 3 which is reproduced in figure 4(a). From the shadowgraph, it is evident that the boundary-layer edge is very irregular. This has been noted by Townsend and by Klebanoff (ref. 13) from hot-wire anemometer observations of a subsonic turbulent boundary layer. The boundary-layer thickness at any station varies with time. For consistency with previously existing wind-tunnel data, the boundary-layer thickness is defined to be that which would be given by a pitot-probe survey; a definition would correspond very nearly to the envelope of maximum thickness. Therefore, the envelope thickness was measured from the shadowgraph (by the method which is described in the appendix), although a few exceptionally thick local disturbances were disregarded where it was felt that they would occur too infrequently to cause much response from a pitot tube. The data thus obtained are shown by the circular symbols and the faired line in figure 10. Also shown are local instantaneous thicknesses from individual fringes in the interferograms, which would be expected to be generally less than the envelope thickness. The envelope from the shadowgraphs should, in fact, correspond to the envelope of the points from the interferograms. From this standpoint, fairly good agreement is shown by the two sets of measurements. A line through the outer points from the interferograms parallel to the curve drawn through shadowgraph data was used to normalize the y coordinate of the density distributions in figure 9.

The use of the envelope thickness of the boundary layer to normalize the y coordinate has the effect of smoothing the connection of the boundary layer to the free stream. Several of the individual density distributions have finite slopes at the outer edge. However, the instantaneous local boundary-layer thickness is usually less than the envelope of thickness, so that the data from individual fringes terminate at y/δ less than 1, in fact as low as 0.78 in figure 9(a). As a result, the mean line of the data in the region of $\rho/\rho_1 = 1.00$ is very nearly of zero slope - that is, the profile of average density is asymptotic to the free-stream density at the boundary-layer edge. A similar effect might be expected to occur in the case of the velocity profile. The data of reference 13 do, in fact, suggest the existence of large instantaneous velocity gradients near the edge of the boundary layer in the subsonic case.

The reduction in density as the wall is approached reflects the increase in static air temperature at the levels in the boundary layer

where the air velocity is low. The model surface temperature, however, is very nearly equal to the boundary-layer-edge temperature for these test conditions, as shown by calculation in the appendix to reference 3. The density ratio at the wall will therefore return to approximately 1. The width of the region in which this reversal of the density curve occurs can be calculated from an estimate of the heat-transfer rate which gives the temperature gradient and hence the density gradient at the wall. From such calculations, it was found that the density minimum should occur near $y/\delta = 0.002$, or at 0.00013 inch from the model surface. This region is therefore of a dimension comparable to the film grain, particularly after demagnification by 4:1, and could not be resolved from the interferograms.

The density distributions obtained from the cone are shown in figure 11 along with the individual fringe shift curves from which they were computed. From this presentation, the effect of the irregularities in the fringe curves can be directly traced. A total of 12 stations were analyzed, 7 from the bottom surface (sheltered side) and 5 from the top (windward side). (The resultant angle of attack was 1.2° , with 1.0° in the plane of the picture.) Nearly all of these density profiles are irregular, with minima near the boundary-layer center or at about one-fourth and three-fourths of the boundary-layer thickness (for example, the second and third ones on the windward side). The probable interpretation of these irregularities is that they represent density variations in individual eddies.

The mean density profiles from the cone, obtained by plotting all of the data of figure 11 onto two curves, one for the sheltered side and one for the windward side, are shown in figure 12. The mean curves obtained, particularly figure 12(a), tend to show a minimum near the boundary-layer center. This may indicate that there are still too few individual surveys in the figure to give a correct average, or it may indicate a real tendency of the density profile to show a minimum near the boundary-layer center.

Comparison With Crocco Equation

A theory which is used to relate the mean density distribution to the mean velocity distribution was derived by Crocco, reference 5. From the observation that the energy and momentum equations of the boundary layer are analogous, Crocco obtained the relation

$$\frac{T}{T_1} = \frac{T_w}{T_1} + \frac{T_s - T_w}{T_1} \frac{u}{u_1} - \left(\frac{T_s}{T_1} - 1 \right) \left(\frac{u}{u_1} \right)^2 \quad (10)$$

(This equation has been derived also by Van Driest (ref. 14) from the equations of motion with fluctuating velocity components.) The density ratios are in turn related to the temperature ratios by the usual assumption of constant static pressure across the boundary layer.

$$\frac{\rho}{\rho_1} = \frac{T_1}{T} \quad (11)$$

The Crocco equation has been checked experimentally from combination of total temperature-probe and pitot-probe surveys, in flight (ref. 6) and in a wind tunnel (ref. 7), with the results shown in figures 13 and 14, respectively. With the exception of the Mach number 8 data from the wind tunnel, these results show substantial agreement of the Crocco equation with experiment. The wind-tunnel data were obtained, however, on the wall of a hypersonic nozzle, with continuous variation in the flow variables outside the boundary layer, and the possibility that the profiles are not "equilibrium" profiles exists particularly at the higher Mach numbers (due to the increase in the rate of variation of the external flow properties with increasing Mach number). Hence, it appears from these data that the Crocco equation is suitable for estimating the density profiles from velocity profiles for boundary layers which have attained equilibrium relative to the external flow.

In the present test, no information on the velocity profile could be obtained. However, on the basis of the large body of available data from pitot surveys of turbulent boundary layers (see, e.g., ref. 7), it seems safe to assume a velocity profile of the power law form,

$$\frac{u}{u_1} = \left(\frac{y}{\delta} \right)^{\frac{1}{n}} \quad (12)$$

Density profiles computed from this assumption by use of equations (10) and (11) are shown overlaid onto the data of figure 12 for $n = 7, 9$, and 11. Similarly computed density distributions for $n = 7$ and 9 are compared with the mean lines of the data from the two ogive-cylinders in figure 15. From these comparisons, it is evident that the density profiles computed are generally similar to those measured. Furthermore, the computed density profiles do not depend sensitively on the choice of the exponent n . Any velocity profile which can be even roughly approximated by a power law distribution with n in the range from 7 to 11 will yield a density distribution comparable to those measured. Conversely, a small variation in the mean density profile will lead to a large variation in the corresponding velocity profile. Therefore, it is not feasible to use equation (10) to predict the velocity profiles accurately from the measured density profiles.

Calculation of the Heat-Transfer Rate

The average rate of heat transfer to the models was computed from the boundary-layer-profile data by use of an energy balance method analogous to the momentum balance method used to obtain average skin friction from data on the mean profiles of density and velocity. From the frame of reference of an observer riding with the model, the air in the boundary layer at the survey station has more thermal energy and less kinetic

energy than it had in the free stream, and part of the initial energy has been taken up by the model in the form of heat. Thus we can write, for the case of an isothermal flat plate,

$$\left(\frac{u_1^2}{2J} + c_p T_1\right) \int_0^\delta \rho u \, dy = \bar{h}(T_r - T_w)x + \int_0^\delta \rho u \left(\frac{u^2}{2J} + c_p T\right) dy \quad (13)$$

expressing in this way the conservation of total energy for the boundary layer with heat transfer. On making this equation dimensionless, it becomes, for the case of constant c_p ,

$$\frac{\bar{h}}{St} \frac{T_r - T_w}{T_1} = \frac{\delta}{x} \left\{ \left(1 + \frac{u_1^2}{2Jc_p T_1}\right) \int_0^1 \frac{\rho}{\rho_1} \frac{u}{u_1} d \frac{y}{\delta} - \int_0^1 \frac{\rho}{\rho_1} \frac{u}{u_1} \left[\left(\frac{u}{u_1}\right)^2 \frac{u_1^2}{2Jc_p T_1} + \frac{T}{T_1} \right] d \frac{y}{\delta} \right\} \quad (14)$$

indicating that from information on the boundary-layer thickness, and the density, temperature, and velocity profiles, the Stanton number can be evaluated. Information on the boundary-layer thickness was obtained by measurement from the shadowgraphs and interferograms. Information on the velocity profiles was obtained by calculations based on the mean skin-friction coefficient, assumed to be known. These procedures will now be described.

Measurement of boundary-layer thickness.—Measurements of boundary-layer thickness on the ogive-cylinder were given in figure 10. Similar measurements were made on the cone and are given in figure 16(a), while the shadowgraph data of figure 10 are repeated on logarithmic coordinates in figure 16(b). It was necessary to evaluate the influence of refraction on these data, and a detailed description of the analysis of refraction that was made is given in the appendix. The results of that study indicated that the boundary-layer thickness should not be measured from shadowgraphs in reference to the apparent position of the model surface, since the surface position was found to be significantly altered by refraction; but should rather be obtained by measuring the over-all diameter at the outer edges of the boundary layer and subtracting the true body diameter to obtain δ . This is the procedure that was used to obtain the shadowgraph data in figures 10 and 16. The interferogram data, however, were obtained by direct measurement of the distance from the model surface to the boundary-layer edge, which is a valid technique in this case because the interferometer camera is in focus on the model and minimizes refraction errors. Comparison of the two sets of data indicates satisfactory agreement and further indicates that the optical errors in the two different optical systems are either fortuitously equal or small. In figure 16(a), the angle of attack of the model in the interferogram was sufficient to cause a measurable difference in boundary-layer thickness on the windward and sheltered sides. However, when envelope thicknesses were drawn for the two sides separately, and the mean of these two envelopes compared to the shadowgraph data, the agreement was excellent.

Evaluation of the velocity profiles.— The velocity profiles were assumed to be represented by the power law, equation (12), so that the evaluation of the velocity profile reduced to evaluating the exponent n . This was done by treating the skin-friction coefficient, which is relatively well established for these test conditions (ref. 4), as known and working the momentum integral method backward to define the velocity profile. The basis of these calculations is the well-known relation between momentum thickness and mean skin-friction coefficient,

$$\frac{\delta}{x} = \frac{C_F/2}{\theta/\delta} \quad (15)$$

As written, equation (15) is applicable to a flat plate in a uniform stream. For a cone, it must be modified as follows:

$$\frac{4\theta}{\delta} \frac{\delta}{x} + \frac{4I}{\tan \phi} \left(\frac{\delta}{x} \right)^2 = C_F \quad (16)$$

where I is a second integral similar to θ/δ and is given by

$$I = \int_0^1 \frac{\rho}{\rho_1} \frac{u}{u_1} \left(1 - \frac{u}{u_1} \right) \frac{y}{\delta} d \frac{y}{\delta} \quad (17)$$

Now θ/δ and I are evaluated by use of the experimental density profiles and power law velocity profiles for several values of the exponent n . The skin-friction coefficient is evaluated by use of the T' method of reference 4 and the Van Driest rule (ref. 15) for turbulent boundary layers on cones. The results of this calculation are shown in figure 16(a). The agreement in slope between the computed curves and the data is good in every case. The agreement in magnitude becomes practically exact for $n = 11$, and this was the value selected in the case of the cone.

Similar treatment was given the ogive-cylinder data. The equation corresponding to equation (16) for a cylinder of radius r with a thick boundary layer is

$$\frac{2\theta}{\delta} \frac{\delta}{x} + \frac{2Ix}{r} \left(\frac{\delta}{x} \right)^2 = C_F \quad (18)$$

Since this is an equation for pure cylinder flow, it was necessary to account for the ogival nose of the model by estimating the length of cylinder required to produce a boundary-layer thickness equal to that at the base of the ogive; accordingly, the values of x were reduced by 1/4 inch. Also corrections were made for the effect of cylinder flow on skin-friction coefficient, consistent with the measurements of reference 16, which indicate a correction of +9 percent to the flat-plate data to obtain C_F at the body base. A parabolic variation of the correction with axial distance was assumed. Values of δ/x thus obtained are shown

in figure 16(b) for $n = 7$ and 8 and may be compared to the least squares fit of the experimental data. The magnitude is fit within 0.002 inch at all stations from $x = 2$ inches to $x = 5$ inches by $n = 8$. The slope does not fit as well as in the case of the cone, but the disagreement in slope is within the accuracy of the experimental data. Hence, the value of n selected for the ogive-cylinder was 8 .

Final calculation of heat-transfer coefficients.— Just as boundary-layer-thickness equations (16) and (18) differed from equation (15), the energy balance equations corresponding to (14) for cones and cylinders with boundary layers thick compared to the body radius will differ from equation (14). Each involves one additional mass-flow integral and one additional energy integral. For the cone, the energy balance leads to

$$\begin{aligned} \overline{St} \frac{T_r - T_w}{T_1} = 2 \frac{\delta}{x} & \left\{ \left(1 + \frac{u_1^2}{2Jc_p T_1} \right) \int_0^1 \frac{\rho}{\rho_1} \frac{u}{u_1} d \frac{y}{\delta} - \int_0^1 \frac{\rho}{\rho_1} \frac{u}{u_1} \left[\left(\frac{u}{u_1} \right)^2 \frac{u_1^2}{2Jc_p T_1} + \frac{T}{T_1} \right] d \frac{y}{\delta} \right\} + \\ & \frac{2}{\tan \Phi} \left(\frac{\delta}{x} \right)^2 \left\{ \left(1 + \frac{u_1^2}{2Jc_p T_1} \right) \int_0^1 \frac{\rho}{\rho_1} \frac{u}{u_1} \frac{y}{\delta} d \frac{y}{\delta} - \int_0^1 \frac{\rho}{\rho_1} \frac{u}{u_1} \left[\left(\frac{u}{u_1} \right)^2 \frac{u_1^2}{2Jc_p T_1} + \frac{T}{T_1} \right] \frac{y}{\delta} d \frac{y}{\delta} \right\} \end{aligned} \quad (19)$$

For the cylinder, it becomes

$$\begin{aligned} \overline{St} \frac{T_r - T_w}{T_1} = \frac{\delta}{x} & \left\{ \left(1 + \frac{u_1^2}{2Jc_p T_1} \right) \int_0^1 \frac{\rho}{\rho_1} \frac{u}{u_1} d \frac{y}{\delta} - \int_0^1 \frac{\rho}{\rho_1} \frac{u}{u_1} \left[\left(\frac{u}{u_1} \right)^2 \frac{u_1^2}{2Jc_p T_1} + \frac{T}{T_1} \right] d \frac{y}{\delta} \right\} + \\ & \frac{x}{r} \left(\frac{\delta}{x} \right)^2 \left\{ \left(1 + \frac{u_1^2}{2Jc_p T_1} \right) \int_0^1 \frac{\rho}{\rho_1} \frac{u}{u_1} \frac{y}{\delta} d \frac{y}{\delta} - \int_0^1 \frac{\rho}{\rho_1} \frac{u}{u_1} \left[\left(\frac{u}{u_1} \right)^2 \frac{u_1^2}{2Jc_p T_1} + \frac{T}{T_1} \right] \frac{y}{\delta} d \frac{y}{\delta} \right\} \end{aligned} \quad (20)$$

Application of the energy balance equations to the data yields the results shown in figure 17. For the cone, the computed average Stanton numbers are shown for a Reynolds number range from 8 to 25 million corresponding to stations between 4 and 12 inches from the tip. The boundary-layer profiles have been assumed to be invariant with Reynolds number over this range. The variations in profile that do occur are expected to be small enough to have only a secondary effect on the results. The Stanton numbers are compared with the average skin-friction coefficients given by use of the T' method modified according to the previously mentioned Van Driest rule for turbulent boundary layer on a cone. According to the modified Reynolds analogy of Colburn, $\overline{St}/C_F = 0.5/Pr^{2/3}$, the ratio \overline{St}/C_F should be 0.622 for air. From the analysis of the cone data, the ratio is found to be 0.55 . This is consistent with figure 9 of reference 8 in indicating that at high Reynolds numbers, the ratio of Stanton number to skin-friction coefficient is somewhat less than the value given by the Colburn equation.

The calculations for the ogive-cylinder give the results at the left of figure 17. Stanton numbers were computed for axial stations from $x = 2$ inches to $x = 5$ inches corresponding to Reynolds numbers from 3.6 million to 9 million. The boundary-layer-thickness data were deliberately taken to be those given by the experimental curve, differing in slope from the computed curve of δ vs. x , although as noted in the preceding section, the computed boundary-layer-thickness curve for $n = 8$ was also a possible fit to the measurements. There is therefore a disagreement in slope between the Stanton number and skin-friction coefficient curves, and a variation in the ratio St/C_F from 0.72 to 0.65, with the preferred values occurring at the higher Reynolds number stations where δ/x is known with greater precision. Again, these values agree, for practical purposes, with the modified Reynolds analogy and the collected data of reference 8.

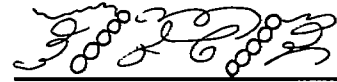
Observations of the Turbulent-Boundary-Layer Image Structure From Shadowgraphs, and Relation to the Interferometer Results

Irregularity of the air density in the turbulent boundary layer is demonstrated more sensitively by shadowgraphs than by the interferometer. This is evident from the shadowgraphs in figure 4. Whereas the interferometer shows the boundary layer only by a relatively small deviation of the fringes, with the irregularities showing up as occasional discontinuities in slope, the shadowgraphs show details of fine structure in the boundary layer. It can be noted that this structure contains recognizable and repeated patterns. In figure 4(a), for example, the basic unit in the pattern is a spot with dark center enclosed in a bright ring. The definition of the spots is in some places quite sharp and in other places more diffuse. The spots are arranged in single-file order back to the station $x/l = 2/3$ beyond which they begin to appear two in depth, usually staggered, and this arrangement persists to the end of the body. The change from single file to two in depth occurs fairly sharply, beginning at a Reynolds number of about 7 million.

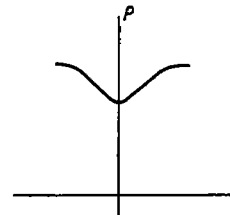
In the shadowgraph of the cone (fig. 4(b)) this same pattern appears although it is less distinct than in the case of the ogive-cylinder. The single-file array of spots is present on the first half of the model and gives way to a more complex arrangement which, on this model, does not appear to be in every case the simple staggered arrangement of two in depth noted in the case of the ogive-cylinder.

A third example is given in figure 18(a). The body shown is a contoured hollow tube from reference 17 with a threaded, continuous V-groove surface transverse to the flow (groove depth = 0.0006 inch). The spot images are in some places quite distinct. The boundary-layer development from the single-file array to the more complex structure is accelerated on this surface. Within a few inches of the origin of turbulence, structures are observed in which as many as six spots can be counted across the thickness of the boundary layer. Furthermore the spots

are found repeatedly arranged in a pattern of the type shown in the adjacent sketch, a diagonal row slanted back in the direction of the free stream at an angle of from 45° to 60° . The space between these patterns is generally filled with more diffuse images, free of distinct spots.



What is the interpretation of these observations? Certainly no quantitative interpretation can be made, in the sense that the interferometer is quantitative. Even a qualitative interpretation is complicated by the fact that the light paths in the boundary layer are of the order of several boundary-layer thicknesses in length, and therefore the light does not respond only to the region near the vertical plane of symmetry. However, it seems plausible to theorize that the spot is the shadowgraph image of an eddy of turbulence. Support is given to this theory by consideration of the light pattern which produces the spot and the type of density distribution which it implies. Light rays are refracted in the direction of increasing air density, so that an axially symmetric distribution of the kind shown in the adjacent sketch would produce a dark center surrounded by a bright ring, the ring occurring where the second derivative departs from zero near the outer edge of the distribution. A central dot having the same brightness as the undisturbed field should also occur. The fact that it is not generally observed would suggest that the density minimum is very sharp. It should be noted, however, that a second type of spot image which has a central dot brighter than the surrounding light field frequently appears (see fig. 18(b)). There would be no effect on the spot image due to superimposing a uniform density gradient such as occurs in the outer portion of the boundary layer with heat transfer. The spot image would be translated but would remain the same within itself.



The correspondence between the density distribution described above and the pressure distribution required to maintain circular motion in a vortex will have been noted by the reader. The pressure distribution and density distribution are exactly similar for isothermal flow. For flows with moderate temperature variations, they would be expected to remain roughly similar. This is the only evidence that indicates that the spot image is an eddy image.

The reasons why the spot image is not destroyed and confused by the long path of the light ray in the boundary layer are not clear. The images are more distinct on the ogive-cylinder, where the ray path length is about $3 \times \delta$, than they are on the slender cone where the path length is about $7 \times \delta$, which would be expected. They are also more distinct in some places than in others, indicating that in some places, only a single eddy appears in the light path, whereas in others, perhaps two or more eddies occur along the path and confuse the pattern.

Subject to the above interpretation, the following things are indicated by the shadowgraphs: The eddy thickness in the turbulent

boundary layer is at first comparable to the boundary-layer thickness. Then a point is reached at which the eddies begin to appear two in depth, and further development leads to as many as six in depth. At this latter stage, the eddies tend to group in backward-slanting patterns, inclined to the surface at from 45° to 60° , separated by a distance comparable to the boundary-layer thickness. The processes described probably occur by rearrangement of the eddies, such as by one climbing over another, rather than by subdivision. This is indicated from the observation that the eddies which initially appear arranged two in depth are comparable in size to the last of those in the single-file order.

These various stages of development of the turbulent boundary layer would be expected to show differences in velocity profile. Now it is well known that the velocity profiles of turbulent boundary layers do not exhibit similarity at all stations, tending to become "fuller" with increasing Reynolds number (see, e.g., ref. 18). The changes in the boundary-layer structure which are described above offer a physical reason for the lack of profile similarity which is observed.

The instantaneous density profiles obtained from the interferogram of the cone contain minima and are therefore consistent with the type of density profile required to produce spot images. Some of the profiles show a single minimum near the boundary-layer center, and others show two minima, one above and one below center. At the stations on the cone where the surveys were made, the latter type of profile would be expected to predominate, although a few single eddies with diameters of the order of the boundary-layer thickness may be found in the shadowgraph.

As was noted at the beginning of this section, the interferometer is not as sensitive as the shadowgraph for showing up the details of the turbulent boundary layer. In the case of the shadowgraph, the sensitivity was sufficient on the ogive-cylinder to show fine detail, and resolution was lost in going to the cone because of the necessity for averaging over longer light paths. With the interferometer, the sensitivity was marginal in the case of the ogive-cylinder, giving a maximum fringe shift of only about 0.6 of the fringe space at $y/\delta = 0$. The discontinuities in slope, while perceptible on close inspection, were not conspicuous and were generally lost by smooth fairing of the fringe measurements. In the case of the cone, the fringe shifts were tripled, and the discontinuities in slope became conspicuous. This advantage was obtained, however, only at the sacrifice of greater spatial averaging along the light ray, as discussed under Accuracy.

CONCLUDING REMARKS

A study of supersonic turbulent boundary layers on small, slender, gun-launched bodies of revolution at Mach numbers of 3.2 and 3.6 at length Reynolds numbers up to 25 million has been described. A Mach-Zehnder interferometer was used to obtain the instantaneous distributions of

density in the boundary layer (subject to some spatial averaging) and values of the boundary-layer thickness. Additional boundary-layer thickness measurements and flow visualization were obtained from shadowgraphs of the models. The averages of the experimental density profiles were compared to those computed from an equation of Crocco, and the indication was that the density profiles measured agreed in magnitude and in general form with those computed, for a considerable range of assumed velocity profiles. Average heat-transfer rates also were computed from the data by means of an energy balance calculation analogous to the momentum survey method of measuring skin friction. It was necessary to assume a power law velocity profile, but the power exponent was evaluated from experimental data. The results of this analysis showed that the modified Reynolds analogy satisfactorily predicted the average heat-transfer rate.

Perhaps the most interesting results were concerned with irregularities of air density in supersonic turbulent boundary layers. The irregularities shown by interference fringes in the boundary layer of the slender cone model appeared to be of a scale comparable in magnitude to the boundary-layer thickness. The density profiles reduced from these fringes showed fluctuations in density which were appreciable compared to the total range of variation in the mean density profiles. A study of the shadowgraph pictures of the boundary layers indicated the presence of repeating patterns of which the basic unit was a spot image. The spot diameters were observed to be comparable to the total thickness of the boundary layer at first. In one case, the single-file order began to convert over to a second arrangement with the spots piled up two in depth, beginning at a length Reynolds number of about 7 million. In another picture, an arrangement was found in which the spots were six deep, and arranged in backward slanting rows. The possibility was discussed that these spots are shadowgraph images of individual eddies, and it is the authors' opinion that this is the case. If so, the above description gives evidence of a series of configurations of the eddies at various stages of development of the boundary layer.

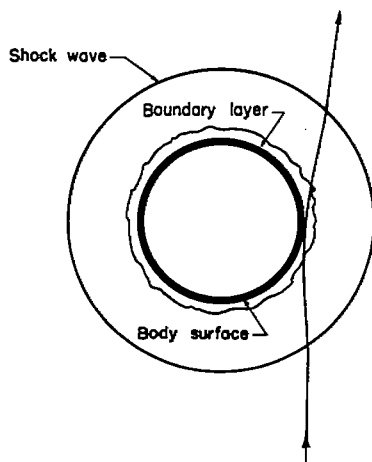
Ames Aeronautical Laboratory
National Advisory Committee for Aeronautics
Moffett Field, Calif., June 17, 1958

APPENDIX

EFFECT OF LIGHT REFRACTION ON THE ACCURACY OF BOUNDARY-
LAYER-THICKNESS MEASUREMENTS FROM SHADOWGRAPHS

Shadowgraphs make flow detail visible by refracting light, and therefore the presence of visible flow details indicates the occurrence of a detectable degree of refraction. Furthermore, measurement of the diameters of test models in shadowgraphs made with precisely parallel light shows them to be enlarged by anywhere from 0.020 inch to 0.090 inch, depending on particular flow conditions. This suggests the existence of appreciable refraction in the flow field, but whether it is due to the boundary layer, shock wave, or intervening region is not apparent. In the present case, it was desired to obtain information on the boundary-layer thickness, and it was therefore necessary to analyze the refraction and to determine whether it would preclude the accurate measurement of boundary-layer thickness from shadowgraphs.

The example chosen for analysis was a picture with considerable distortion of the model diameter, 0.089-inch enlargement. This was observed on a skin-friction model with a turbulent boundary layer and a blunted leading edge from the investigation of reference 4. The model is indicated schematically in cross section in the sketch at the left. First it was determined by calculation and also by measurement of shadow pictures of the model at rest in still air that the effect of wave diffraction was to enlarge the shadow diameter by about 0.020 inch (for the particular model-to-film distances employed). This, then, would be the minimum distortion. Then three sources of refraction which would bend the light rays in the directions indicated on the sketch were considered. On entering and leaving the disturbed flow region, that is, on crossing the shock wave, the rays are bent inward, in such a direction as to decrease the apparent diameter. From measurements of the wave angle, the density ratio across the shock wave was determined. By application of Snell's law of refraction, it was found that the body diameter would, for this example, be decreased in the picture by 0.002 inch. Hence, this effect was not only of the wrong magnitude but also of the wrong direction to produce the observed enlargement. Next, the refraction in the disturbed flow field outside the boundary layer was computed, by use of a density distribution reduced from an interferogram of the model. This refraction tended to enlarge the model diameter by 0.004 inch total, so that the combined effect of the shock wave and flow field external to the boundary layer was to enlarge the diameter by 0.002 inch. The remaining source of refraction was the boundary layer. Note in the sketch that



the ray path in the boundary layer is comparable to that in the external flow field, and the density gradients are very nearly normal to the ray, which is a requirement for producing refraction. Also the density gradients in the boundary layer are larger than in the external flow. The computed distortion at the film on the ray which passes just outside the point in the boundary layer where the density is minimum was from 0.040 to 0.060 inch depending on the value of density gradient chosen, there being some uncertainty of the slope of the density curve in this region. (Note that the distortion at the film is amplified by the long "lever arm" distance from the model to the film. Refraction can therefore be important in this case and simultaneously negligible in the interferometer.) Combining the above distortion with the diffraction gives a total enlargement of diameter which agrees in magnitude with that observed. Hence it is concluded that meaningful position measurements cannot be obtained in the shadowgraphs using rays which pass through the boundary layer.

The ray which is tangent to the boundary-layer edge, however, is not subject to the boundary-layer distortions and is, in fact, subject to a gross distortion of only 0.002 inch for the example chosen. Therefore a measurement from the edge of the boundary layer to the corresponding edge on the other side of the body should be a valid measurement of $d + 2\delta$ from which the true body diameter may be subtracted to give measured values of δ .

REFERENCES

1. Zobel, Th.: Flow Measurement by Means of Light Interference. NACA TM 1253, 1949.
2. Blue, Robert E.: Interferometer Corrections and Measurements of Laminar Boundary Layers in Supersonic Stream. NACA TN 2110, 1950.
3. Jedlicka, James R., Wilkins, Max E., and Seiff, Alvin: Experimental Determination of Boundary-Layer Transition on a Body of Revolution at $M = 3.5$. NACA TN 3342, 1954.
4. Sommer, Simon C., and Short, Barbara J.: Free-Flight Measurements of Turbulent-Boundary-Layer Skin Friction in the Presence of Severe Aerodynamic Heating at Mach Numbers From 2.8 to 7.0. NACA TN 3391, 1955.
5. Crocco, Luigi: Transmission of Heat From a Flat Plate to a Fluid Flowing at a High Velocity. (L'Aerotecnica, vol. XII, no. 2, Feb., 1932) NACA TM 690, 1932.
6. Swanson, Andrew G., Buglia, James J., and Chauvin, Leo T.: Flight Measurements of Boundary-Layer Temperature Profiles on a Body of Revolution (NACA RM-10) at Mach Numbers From 1.2 to 3.5. NACA TN 4061, 1957.
7. Lobb, R. Kenneth, Winkler, Eva M., and Persh, Jerome: NOL Hypersonic Tunnel No. 4 Results VII: Experimental Investigation of Turbulent Boundary Layers in Hypersonic Flow. NAVORD Rep. 3880, U. S. Naval Ordnance Lab., White Oak, Md., Mar. 1955.
8. Seiff, Alvin: Examination of the Existing Data on the Heat Transfer of Turbulent Boundary Layers at Supersonic Speeds From the Point of View of Reynolds Analogy. NACA TN 3284, 1954.
9. Stalder, Jackson R., and Seiff, Alvin: The Simulation and Measurement of Aerodynamic Heating at Supersonic and Hypersonic Mach Numbers. Presented at the Seventh Meeting of the Wind Tunnel and Model Testing Panel, Ottawa, Canada, AG19/P9, June 1955.
10. Seiff, Alvin: A Free-Flight Wind Tunnel for Aerodynamic Testing at Hypersonic Speeds. NACA Rep. 1222, 1955.
11. Ladenburg, R., van Voorhis, C. C., and Winckler, J.: Interferometric Study of Supersonic Phenomena. Part I. NAVORD Rep. 69-46, Apr. 17, 1946.
12. Winkler, Ernst H.: Analytical Studies of the Mach-Zehnder Interferometer, Part II. NOL Rep. 1099, U. S. Naval Ordnance Lab., White Oak, Md., Feb. 20, 1950.

13. Klebanoff, P. S.: Characteristics of Turbulence in a Boundary Layer With Zero Pressure Gradient. NACA Rep. 1247, 1955. (Supersedes NACA TN 3178)
14. Van Driest, E. R.: Turbulent Boundary Layer Flow in Compressible Fluids. Jour. Aero. Sci., vol. 18, no. 3, Mar. 1951, pp. 145-160, 216.
15. Van Driest, R. R.: Turbulent Boundary Layer on a Cone in a Supersonic Flow at Zero Angle of Attack. Jour. Aero. Sci., vol. 19, no. 1, Jan. 1952, pp. 55-57, 72.
16. Chapman, Dean R., and Kester, Robert H.: Turbulent Boundary-Layer and Skin-Friction Measurements in Axial Flow Along Cylinders at Mach Numbers Between 0.5 and 3.6. NACA TN 3097, 1954. (See also Jour. Aero. Sci., vol. 20, no. 7, July 1953, pp. 441-448)
17. James, Carlton S.: Observations of Turbulent Burst Geometry and Growth in Supersonic Flow. NACA TN 4235, 1958.
18. Persh, J.: A Theoretical Investigation of Turbulent Boundary Layer Flow With Heat Transfer at Supersonic and Hypersonic Speeds. NAVORD Rep. 3854, May 19, 1955.

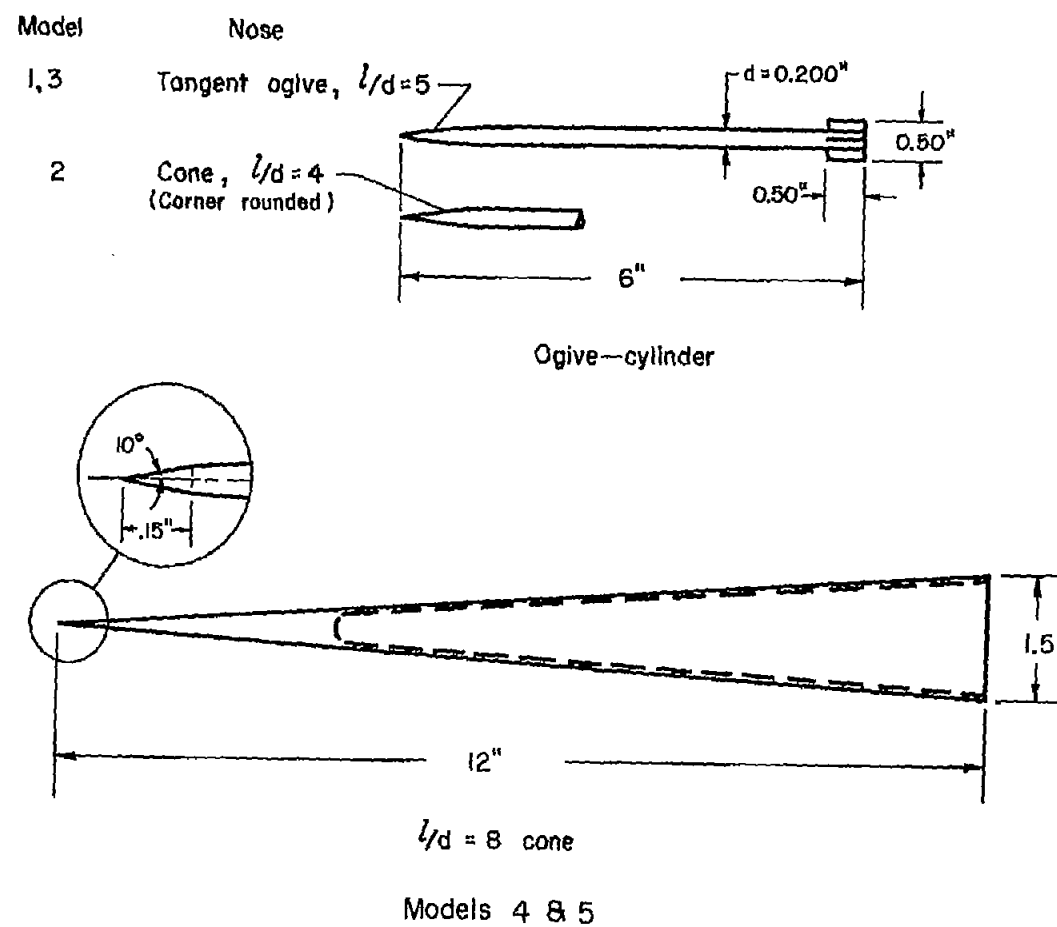
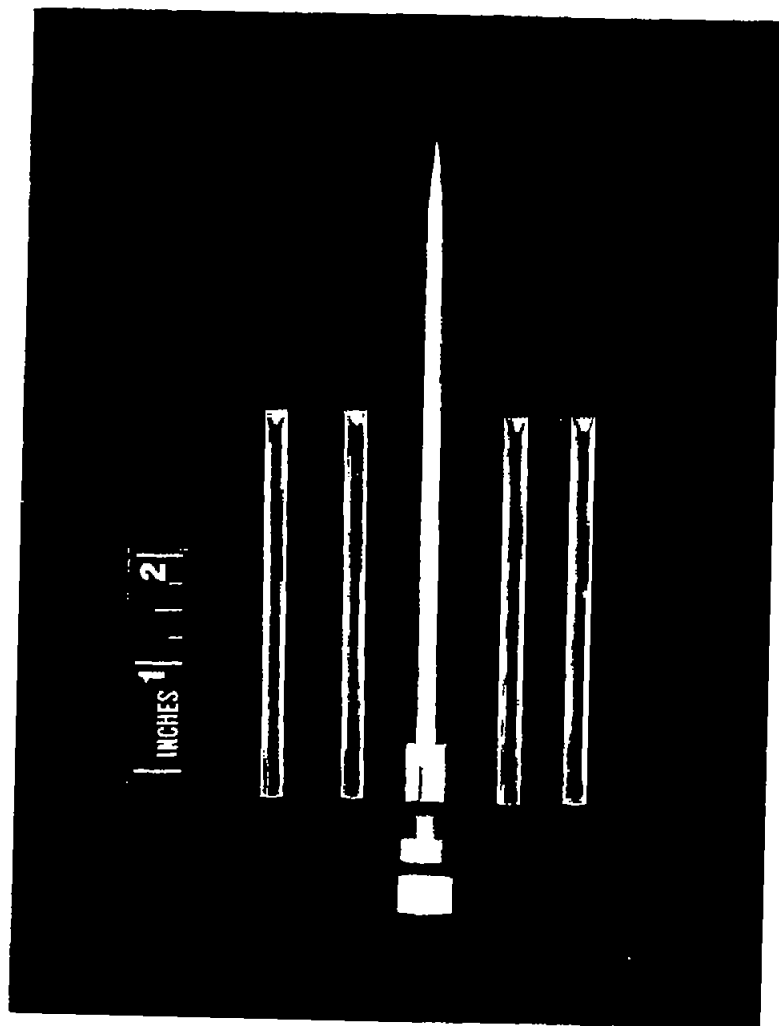
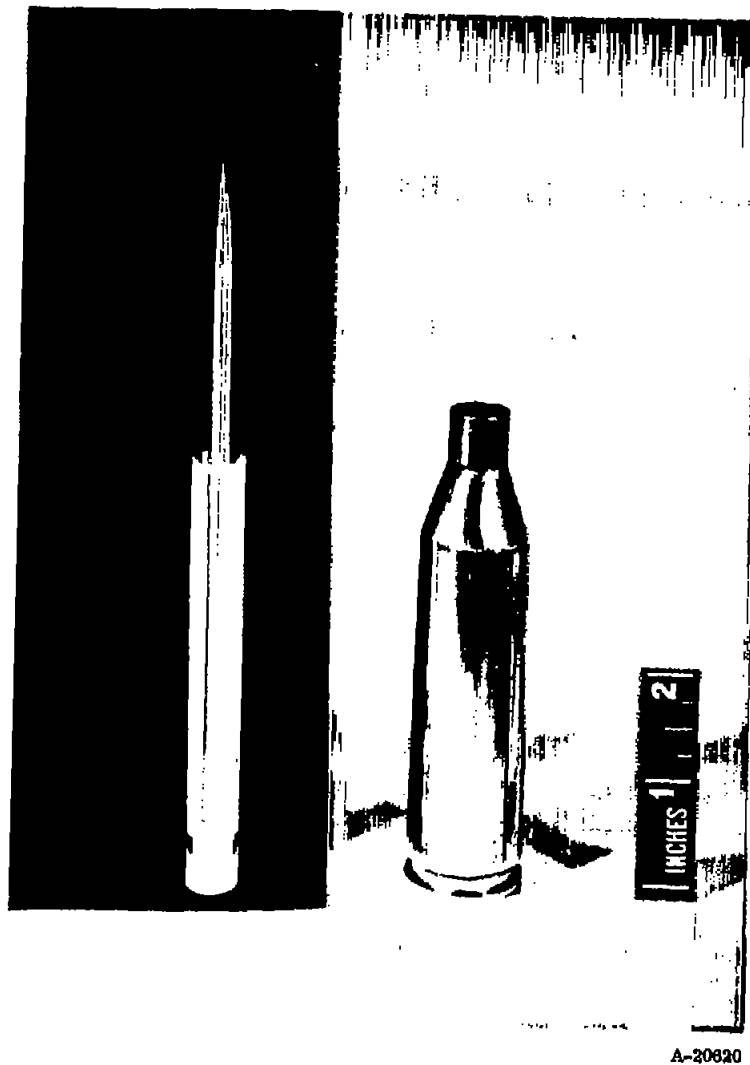


Figure 1.- Sketches of test models.



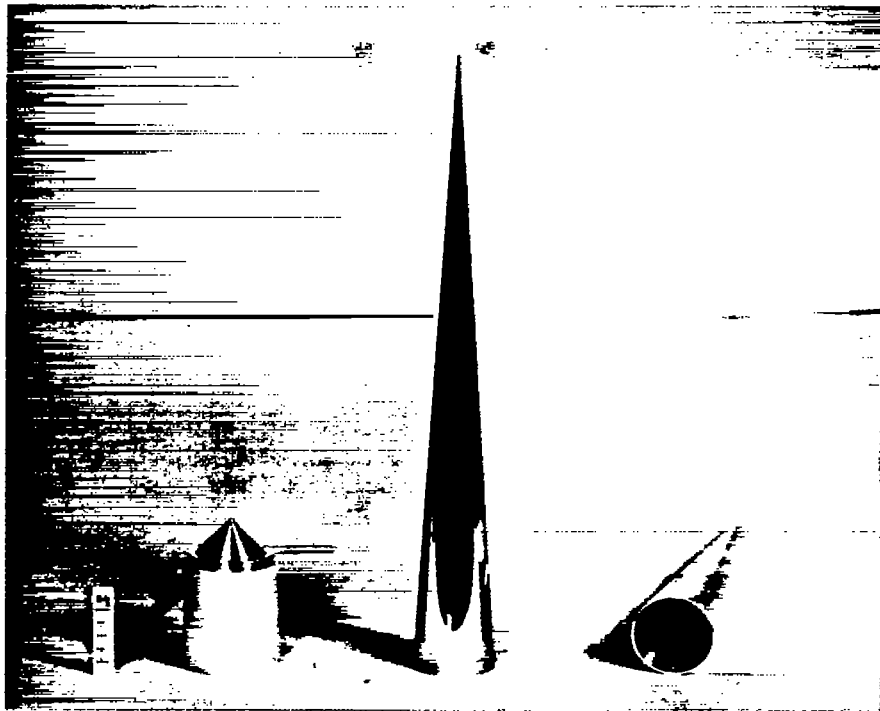
A-20819

(a) Ogive-cylinder.

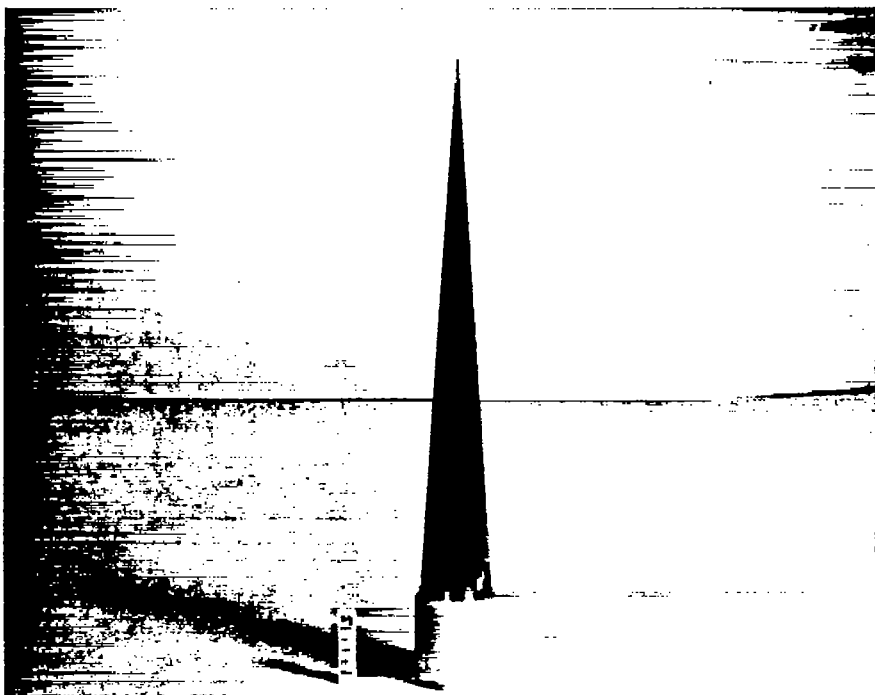


A-20820

Figure 2. - Photographs of models and sabots.



A-20238



(b) Cone.

A-20239

Figure 2. - Concluded.

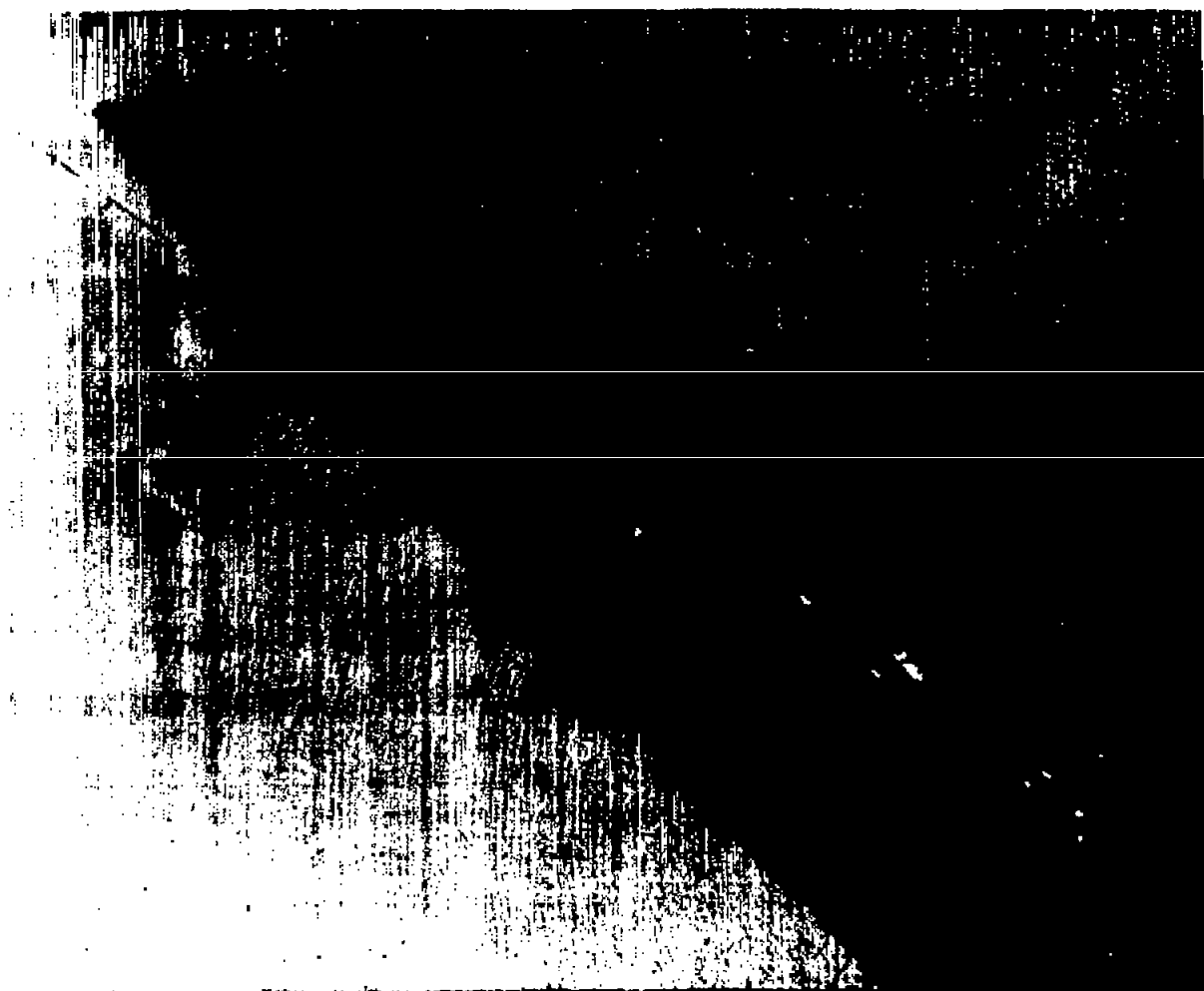
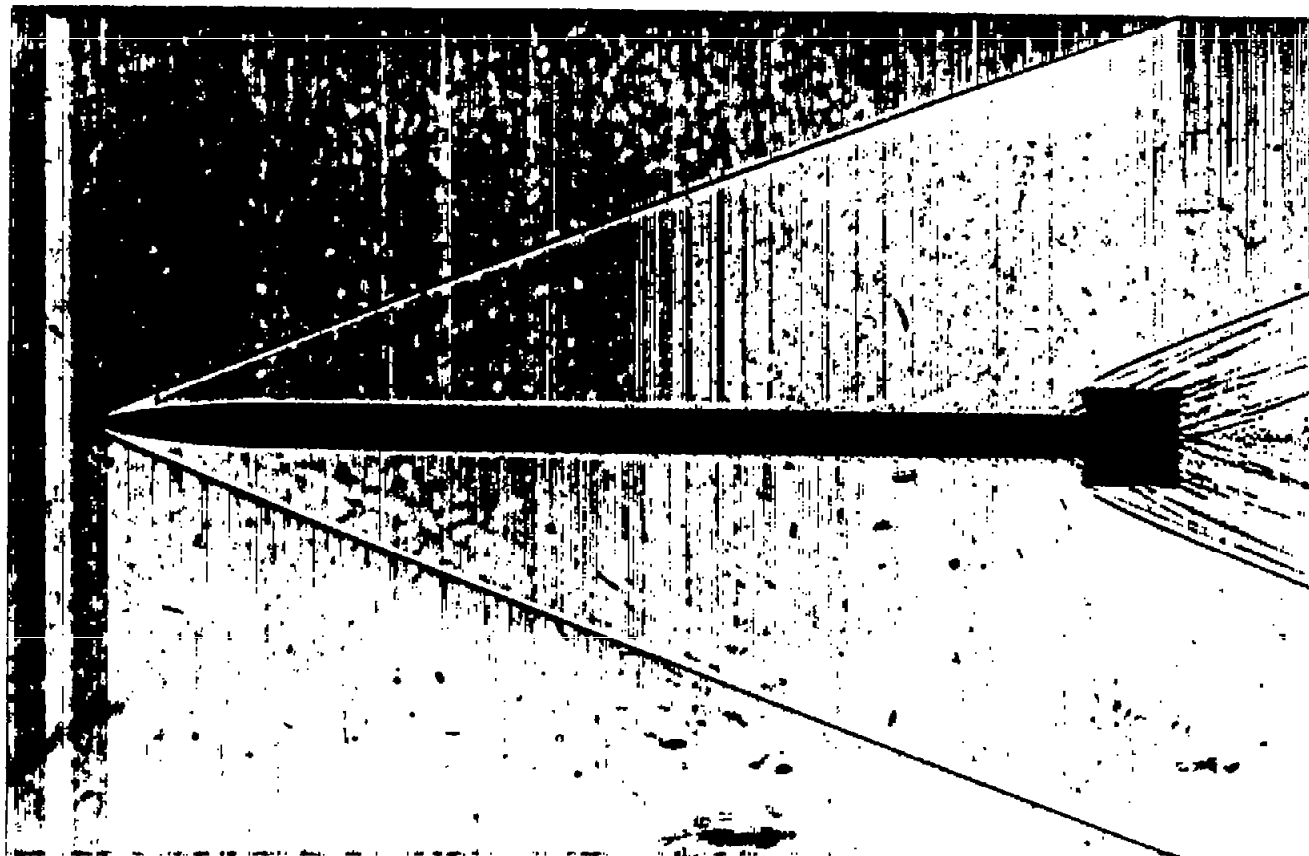


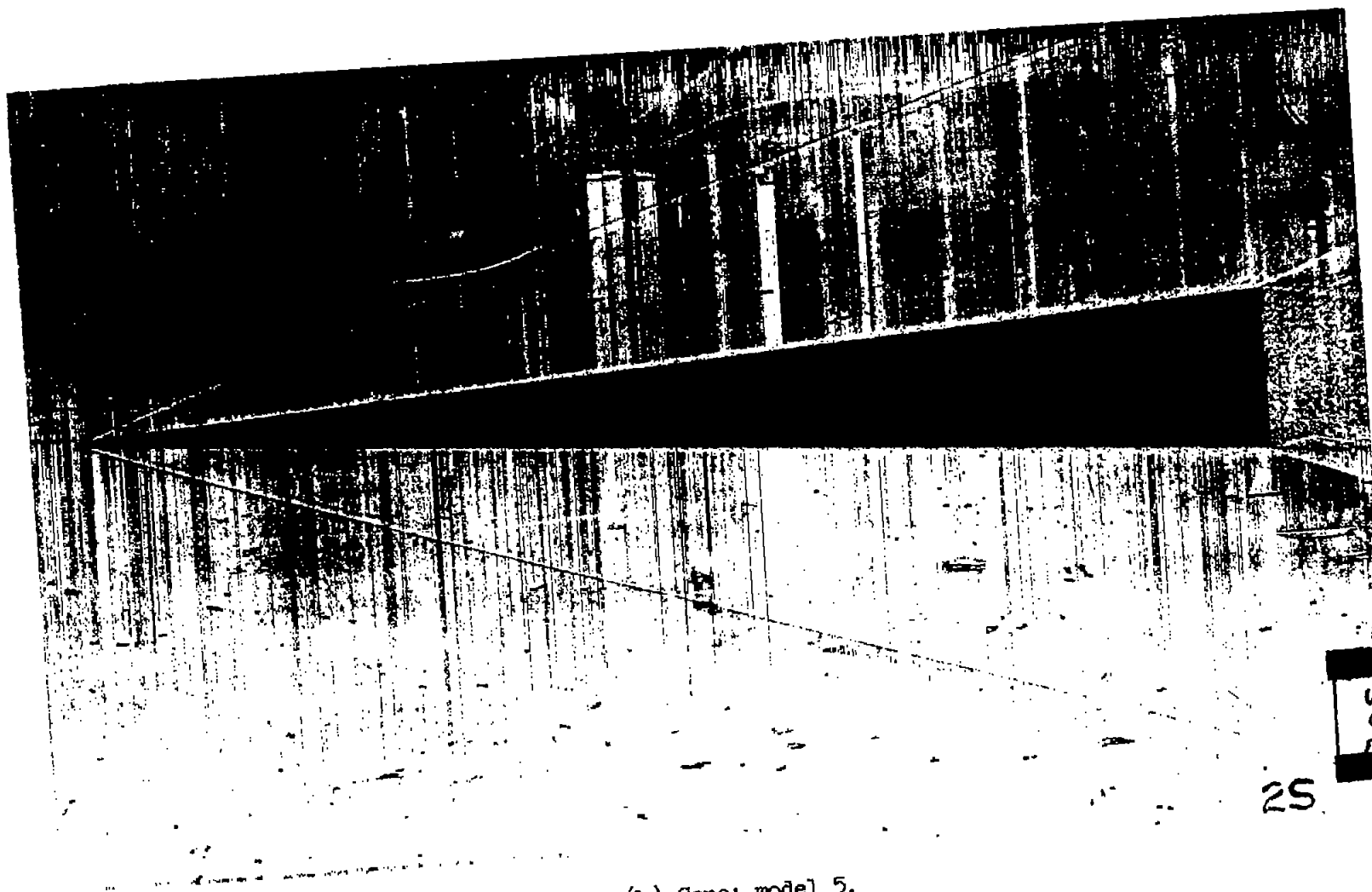
Figure 3.- Photomicrograph at 100X of the boundary-layer trip region on the ogive-cylinder; model 1.



(a) Ogive-cylinder; model 3.

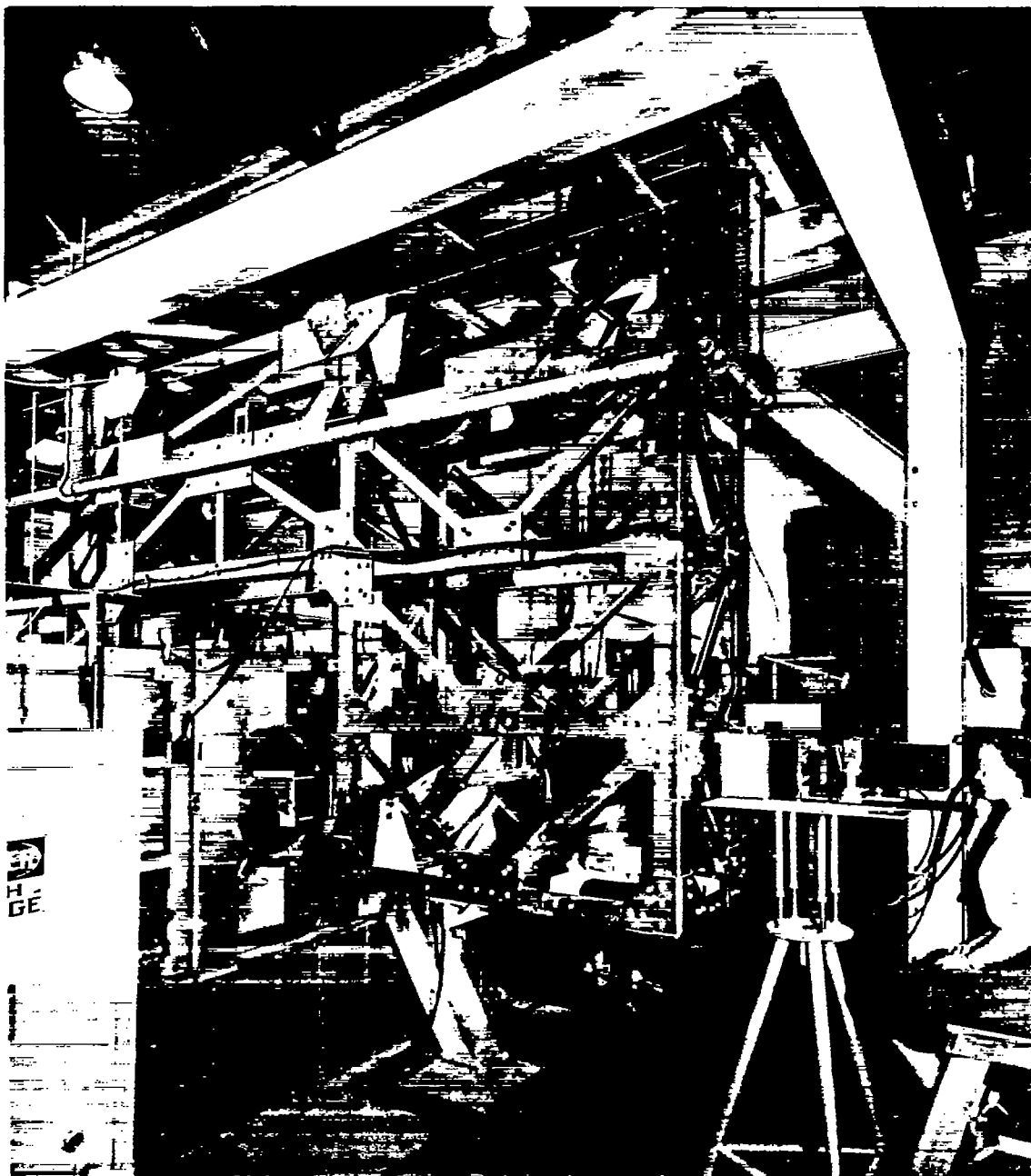
A-21773

Figure 4.- Shadowgraphs.



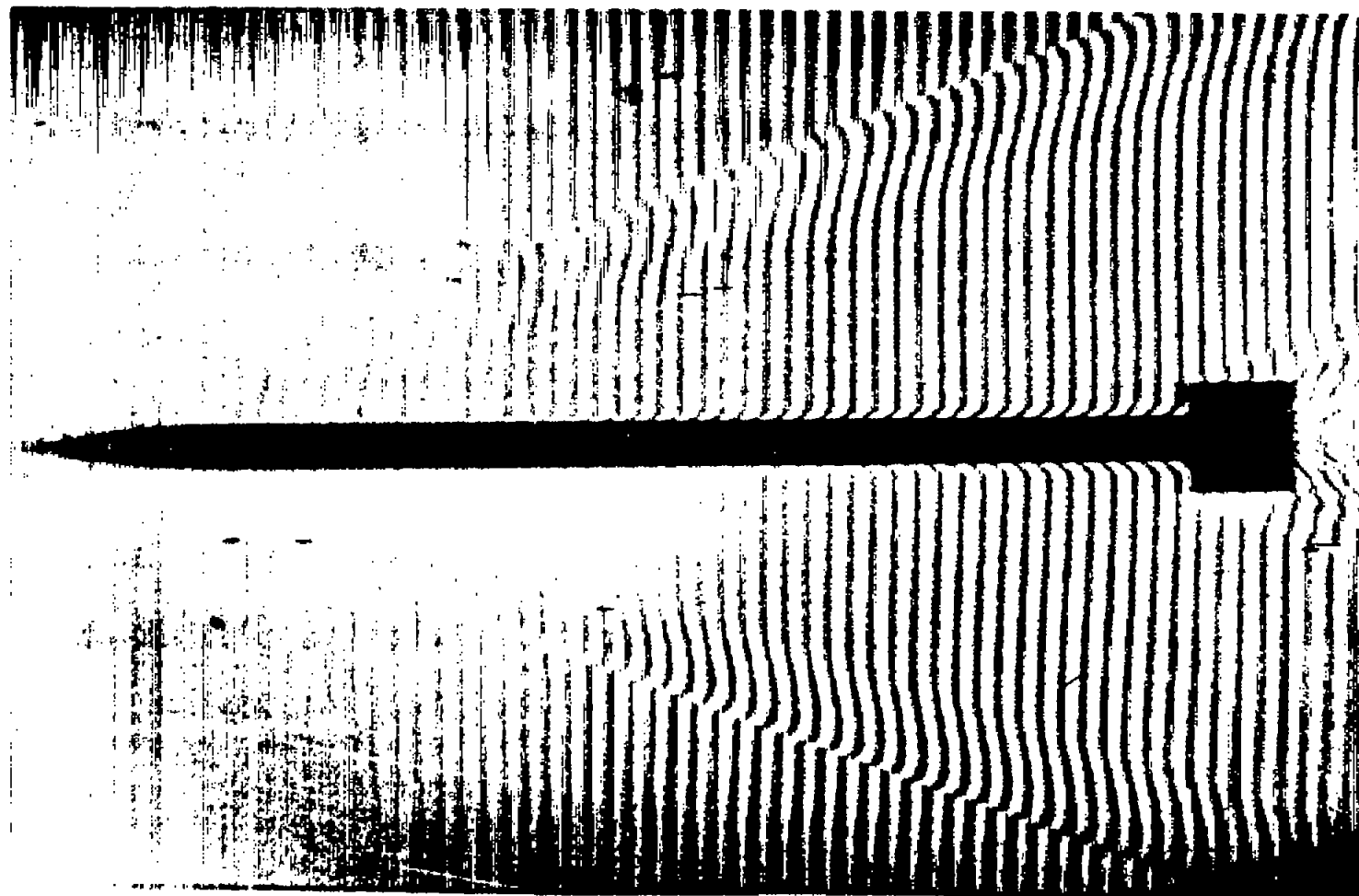
(b) Cone; model 5.

Figure 4.- Concluded.



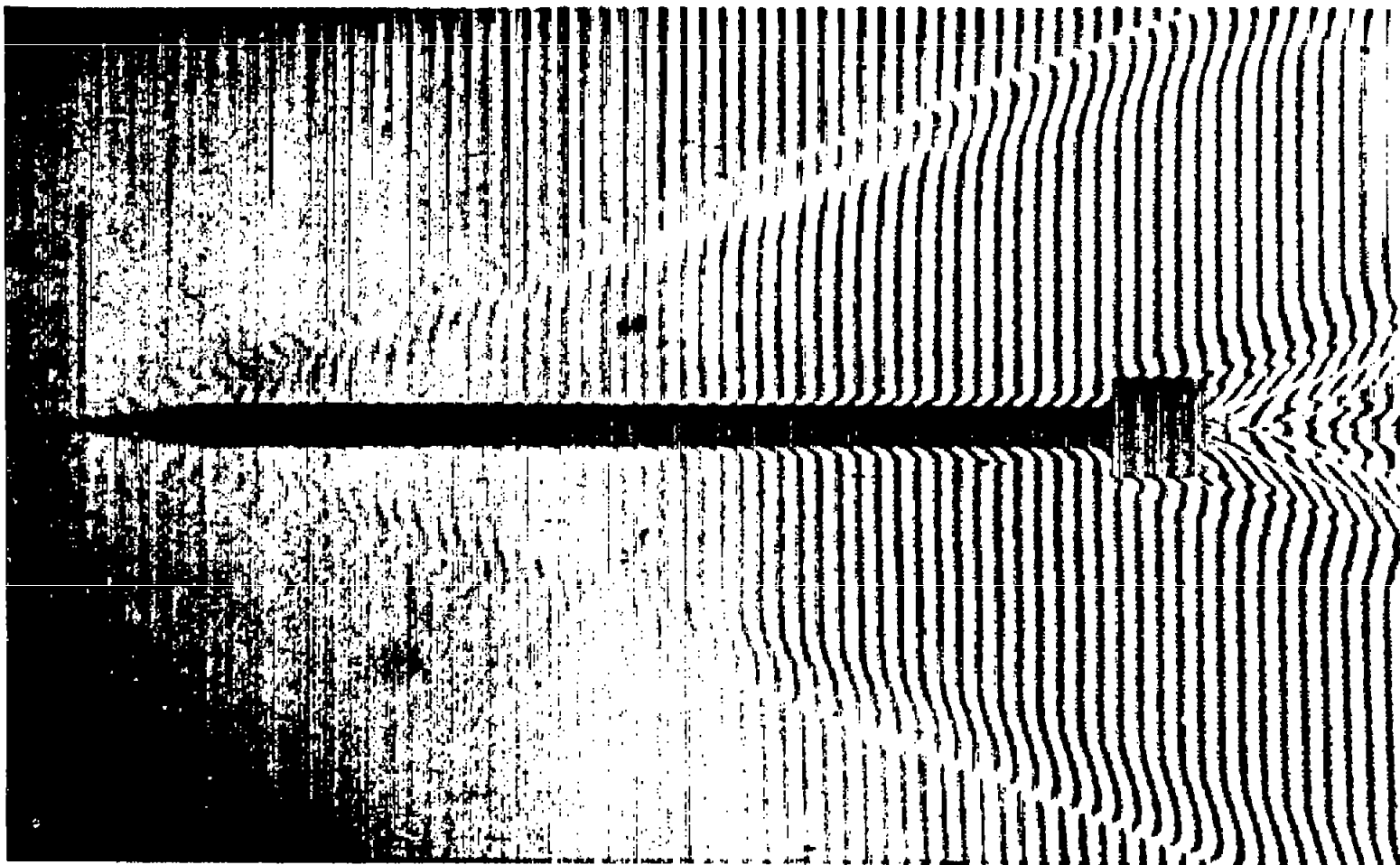
A-23376

Figure 5.- Interferometer in place on the wind tunnel; viewed from the camera side.



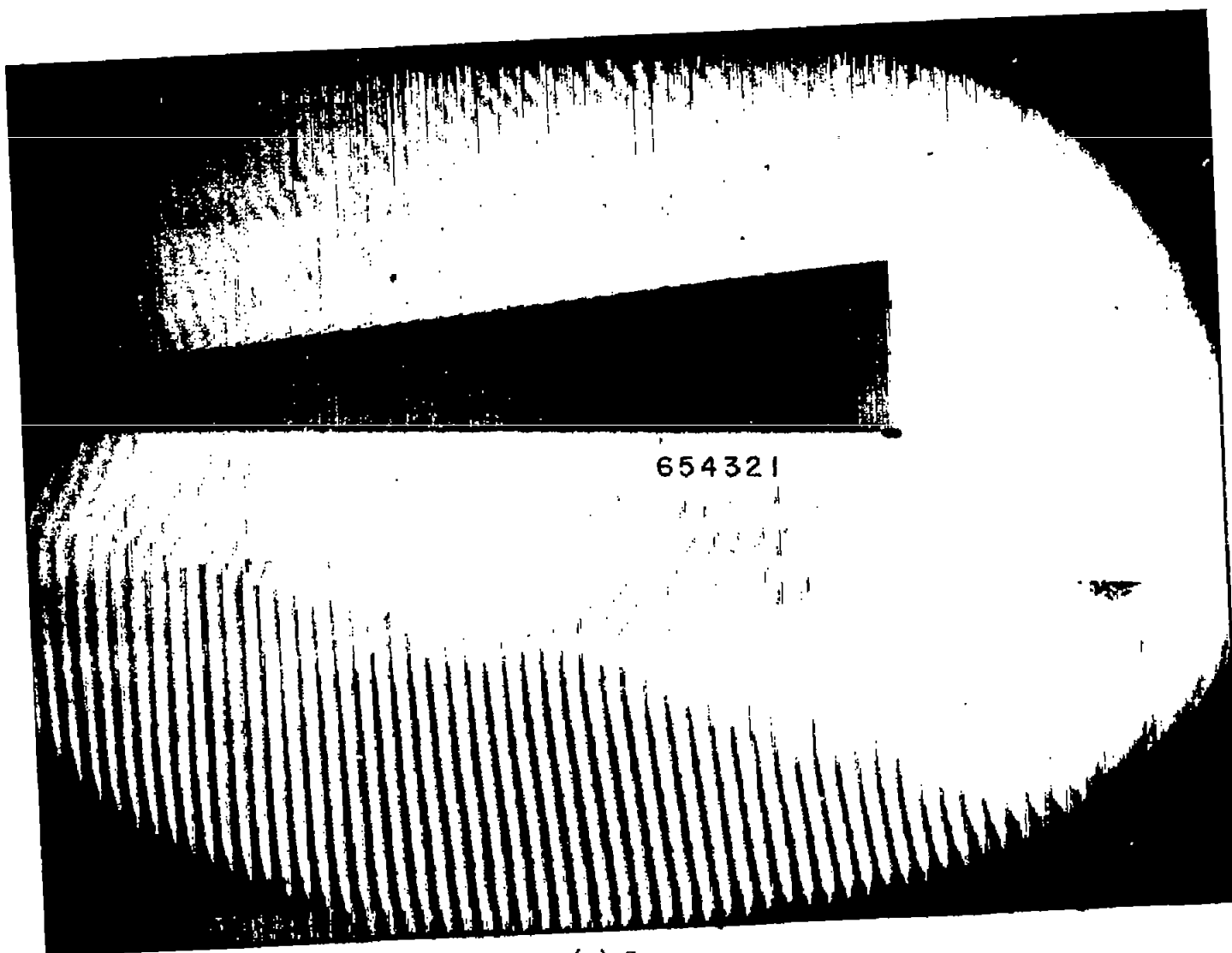
(a) Ogive-cylinder Number 1.

Figure 6.- Interferograms.



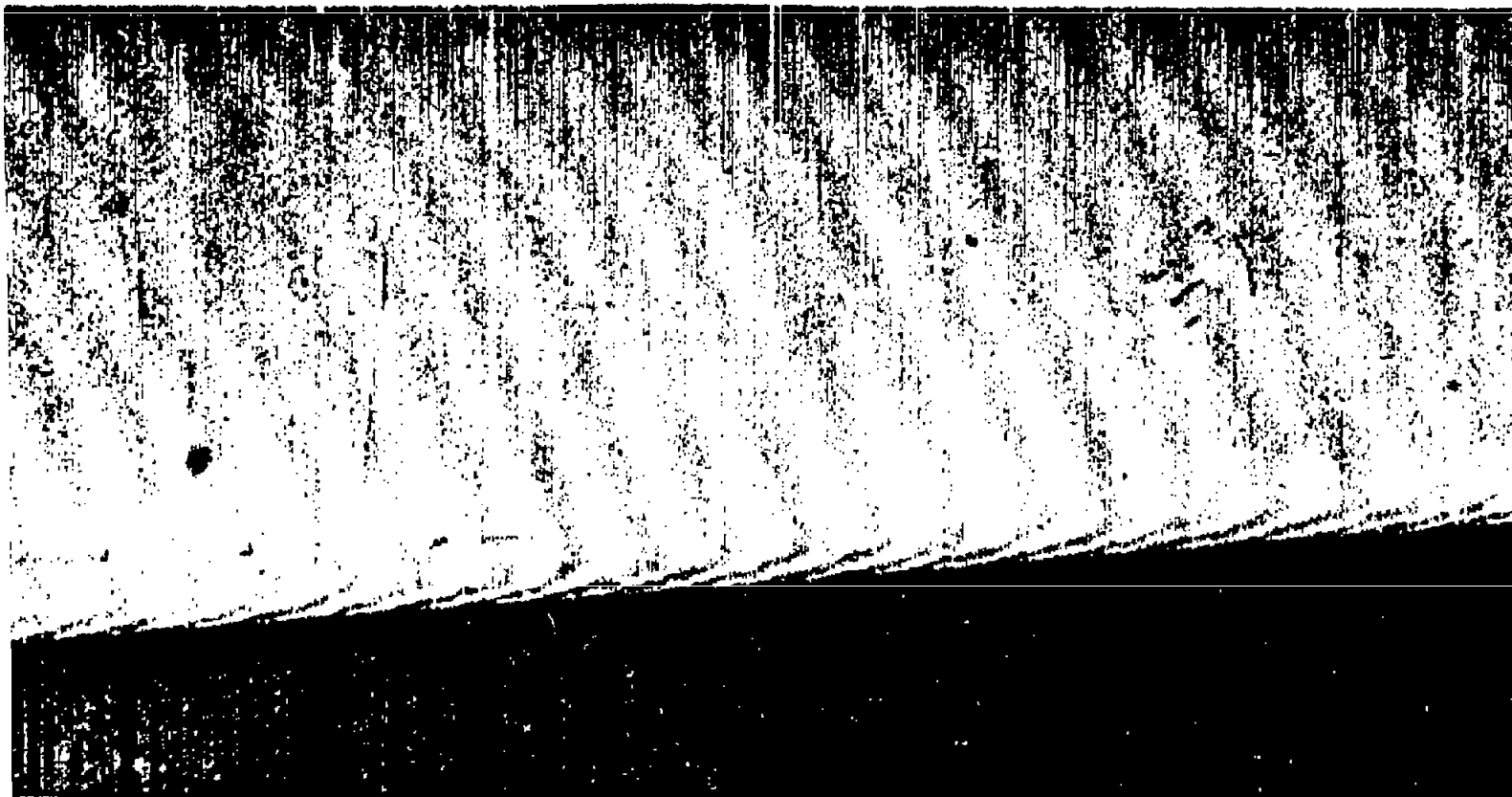
(b) Ogive-cylinder Number 2.

Figure 6.- Continued.



(c) Cone.

Figure 6.- Continued.



(d) Enlargement of fringes from the sheltered side of the cone.

Figure 6.- Concluded.

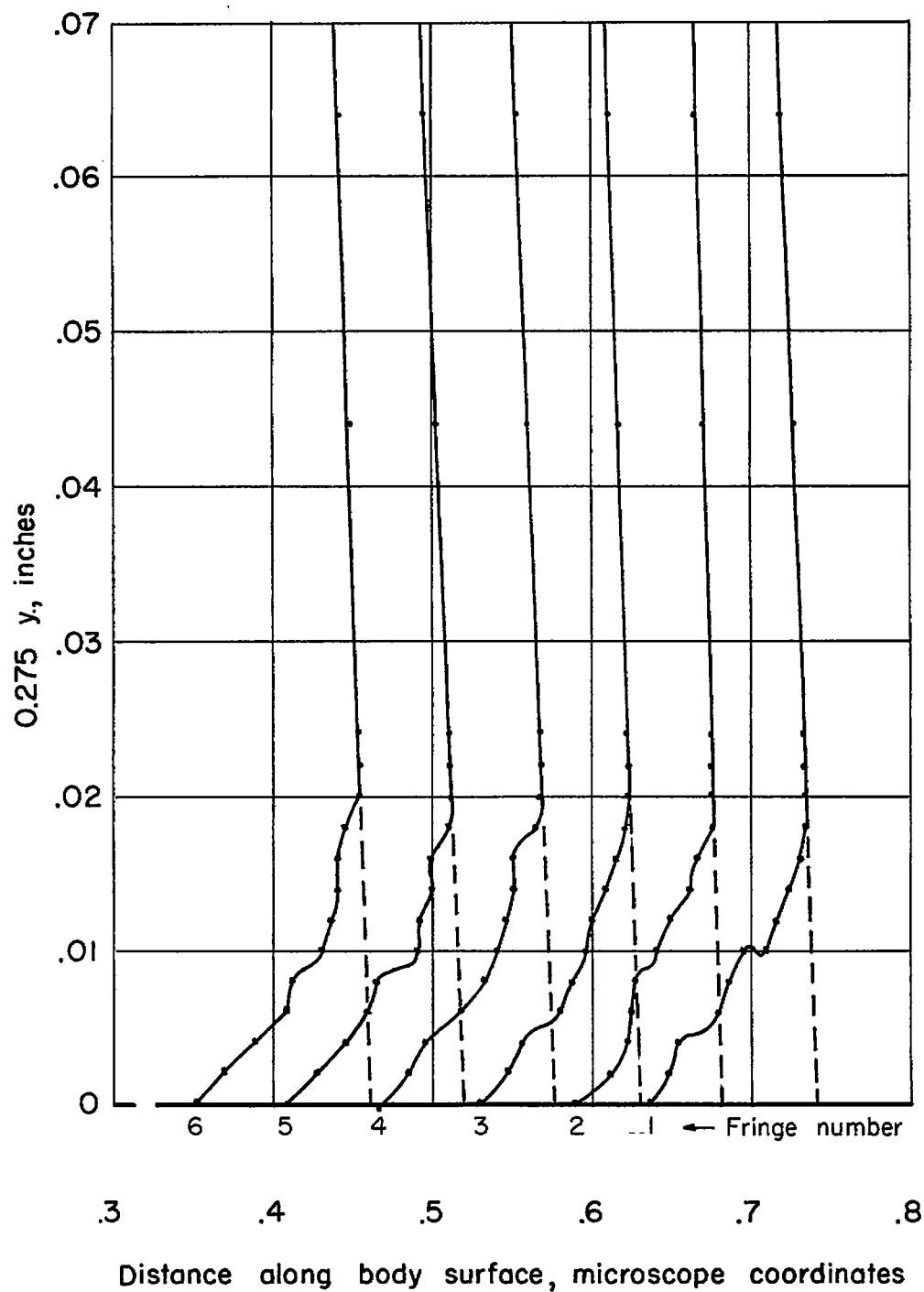


Figure 7.- Coordinates of boundary-layer fringes on the cone;
magnification = 0.275.

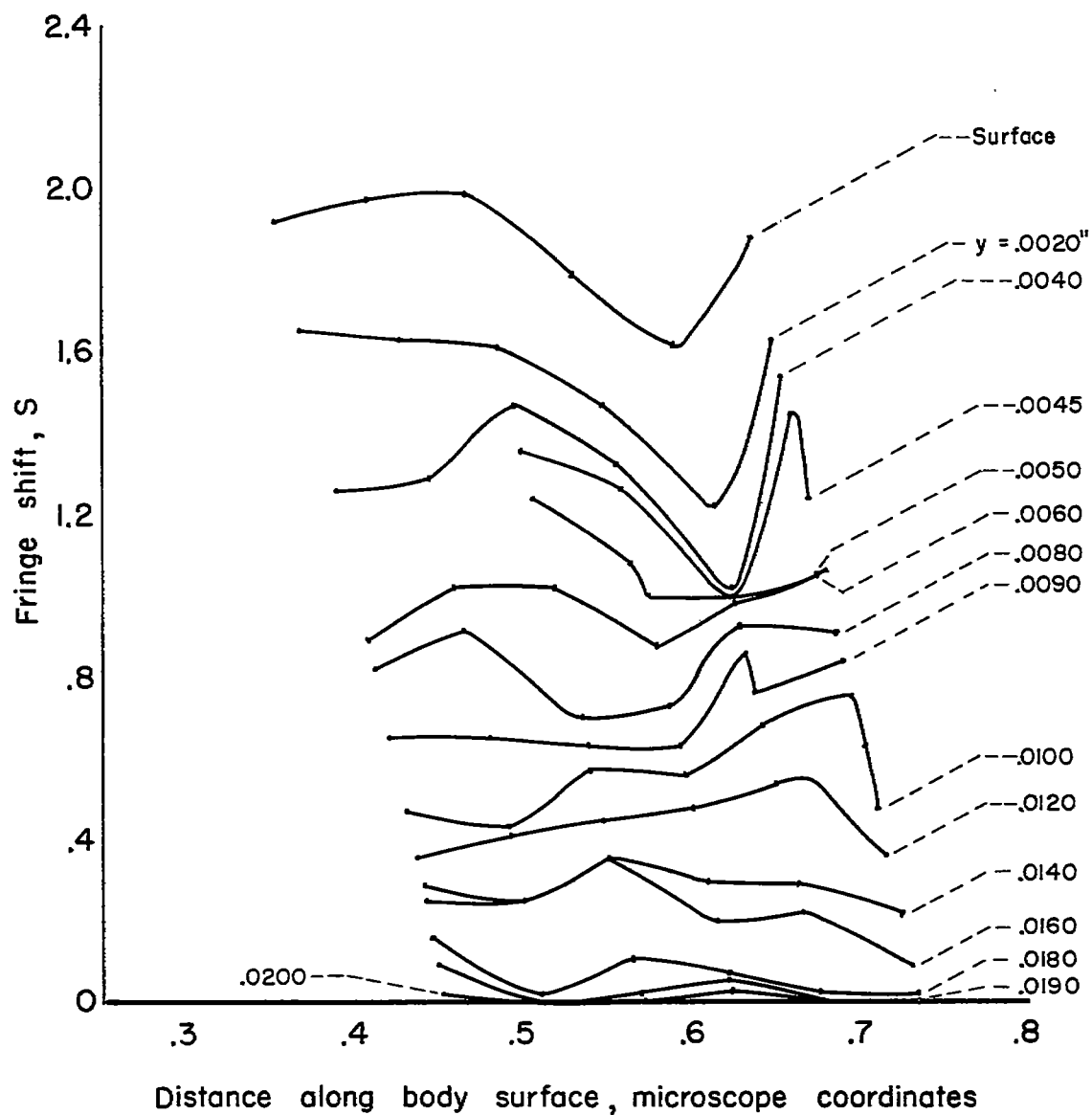


Figure 8.- Variation of fringe shift with x at constant distance above the surface; data of figure 7.

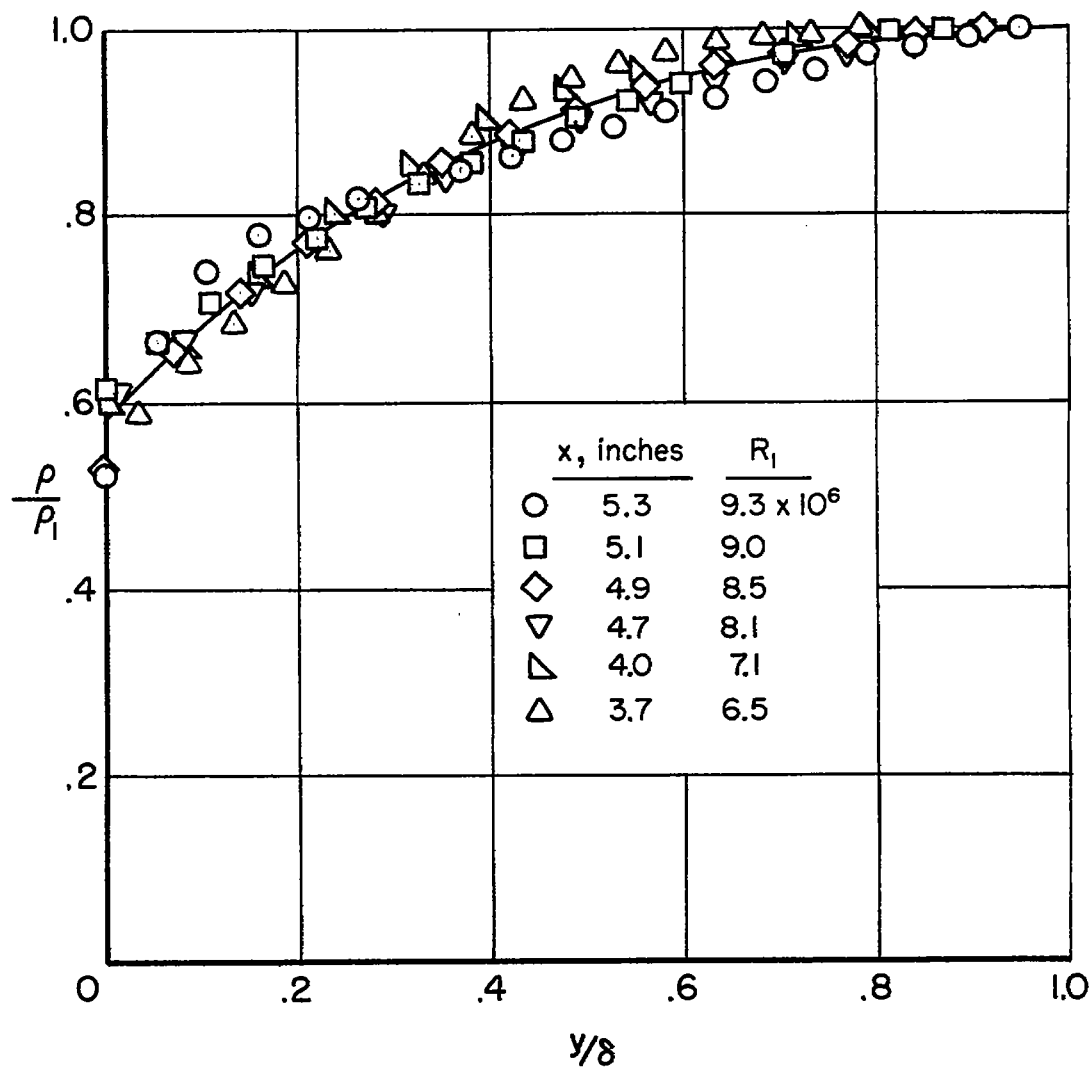
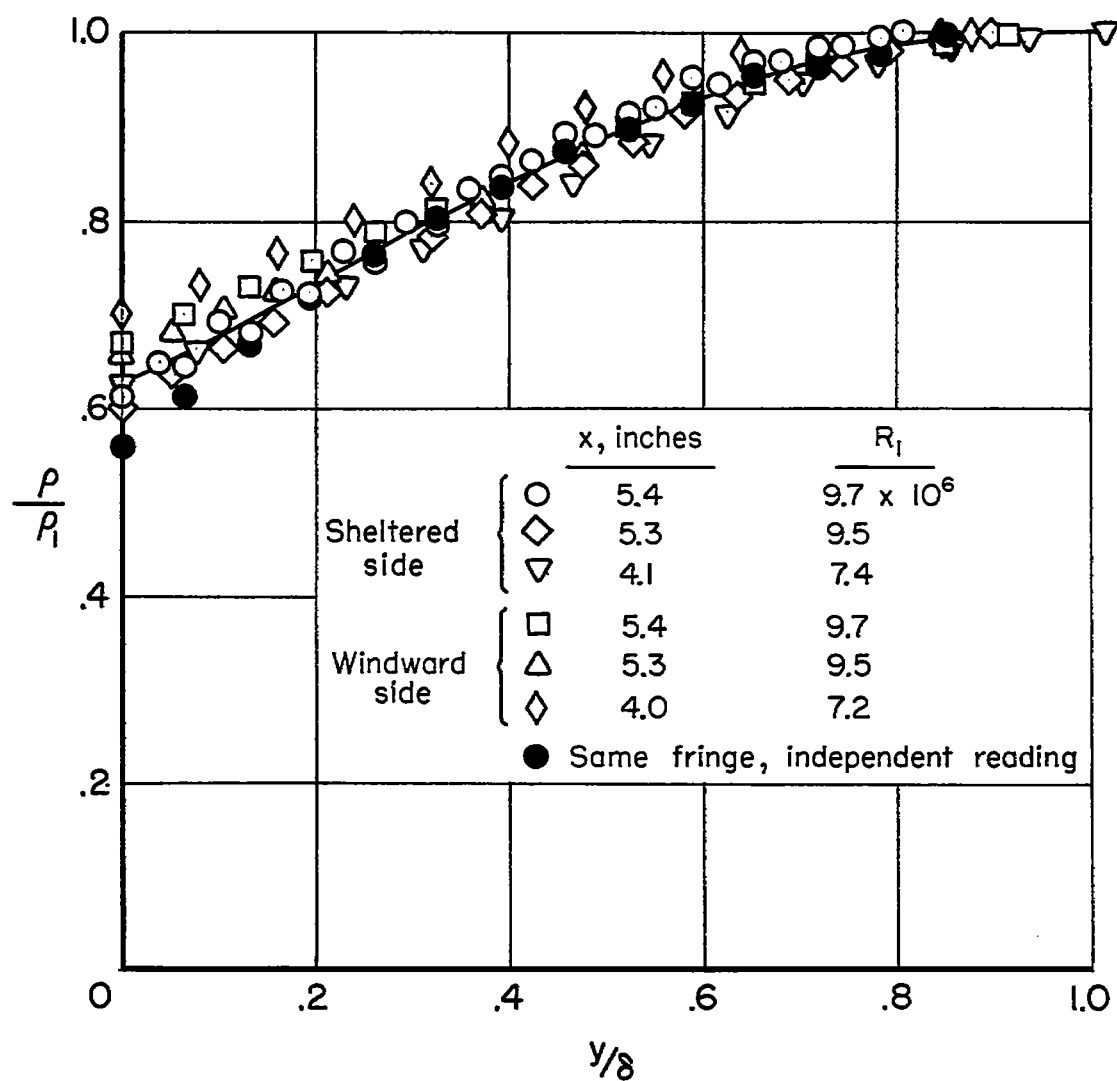
(a) Model 1; $M_1 = 3.15$.

Figure 9.- Dimensionless density profiles from the ogive-cylinders.



(b) Model 2; $M_1 = 3.21$.

Figure 9.- Concluded.

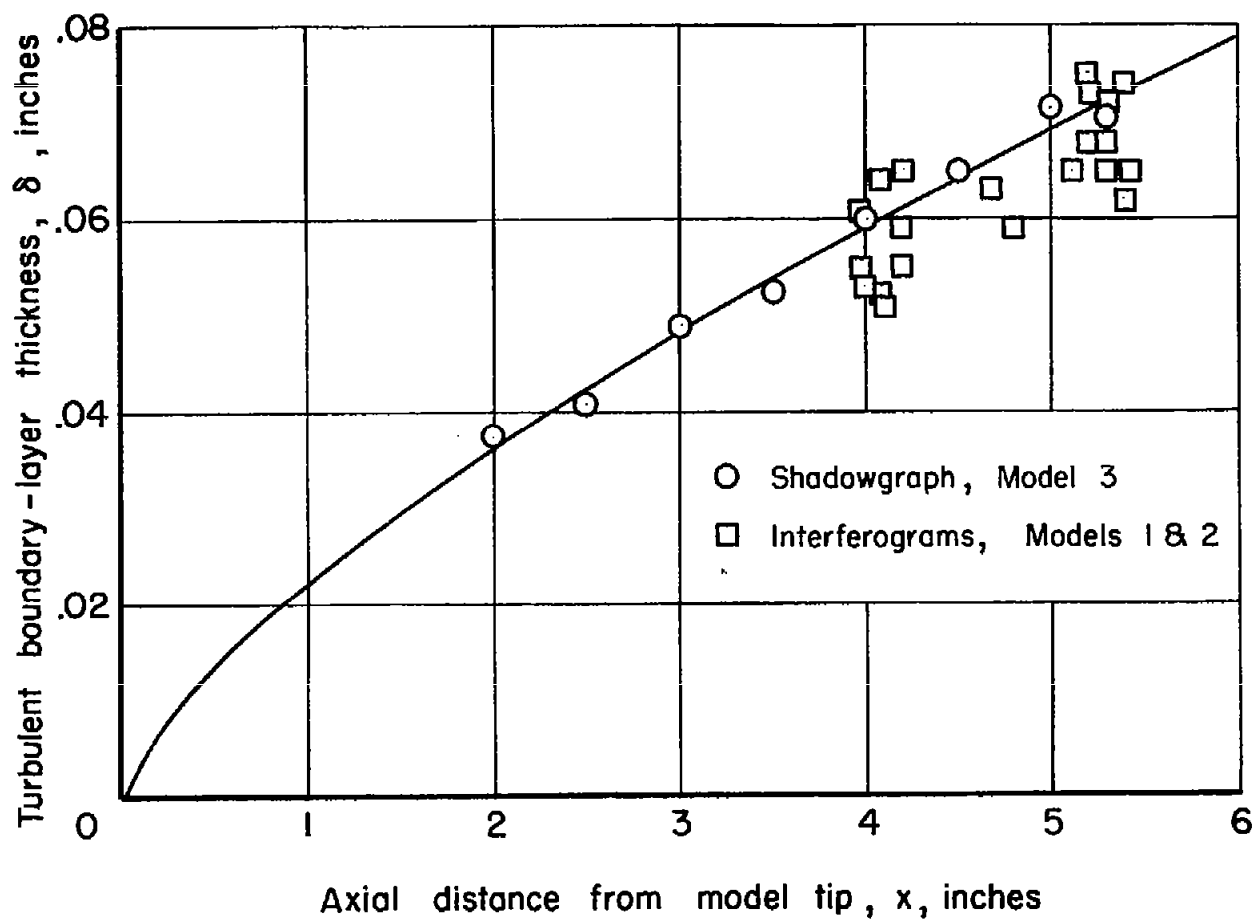


Figure 10.- Boundary-layer thickness data from the ogive-cylinders.

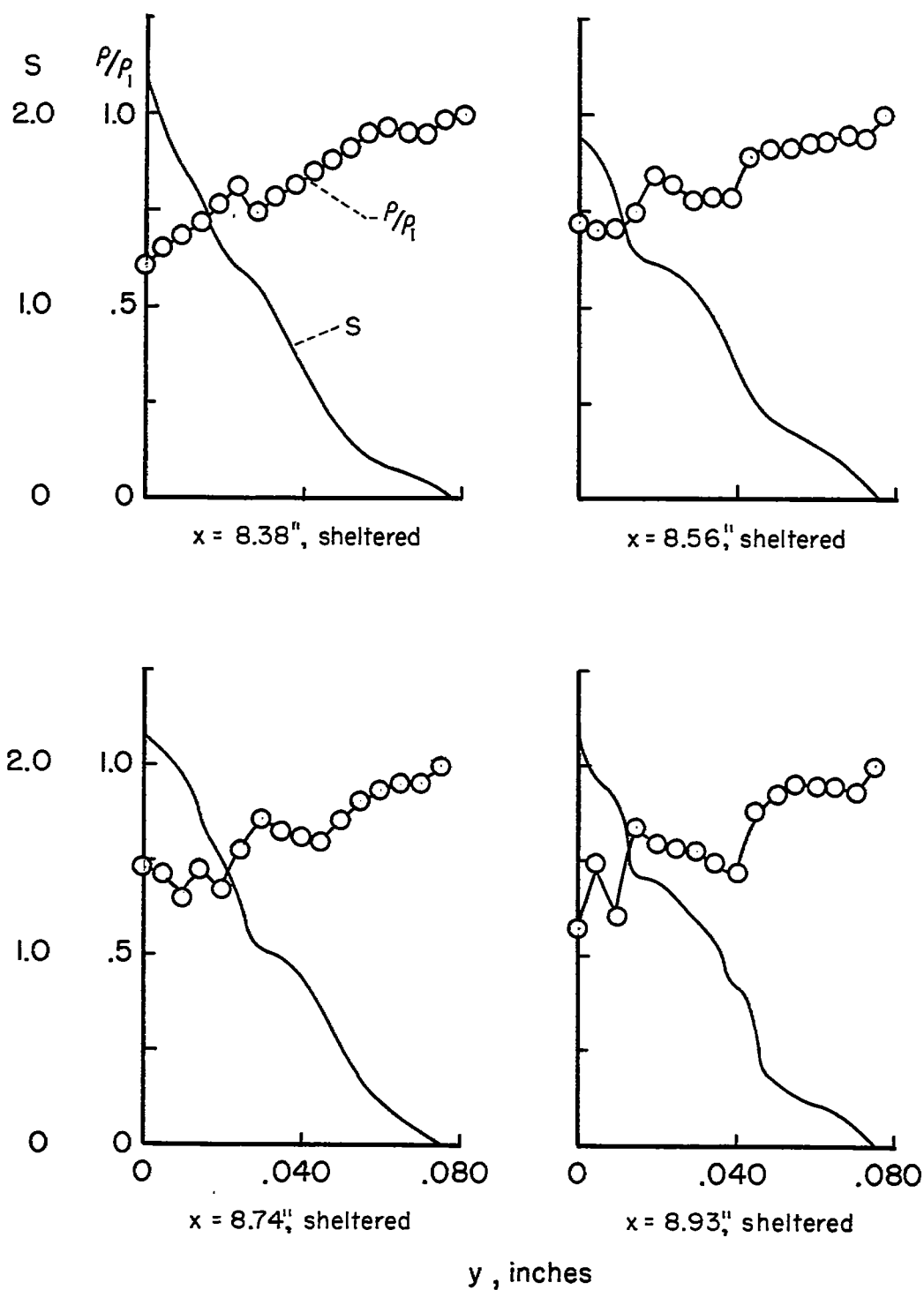


Figure 11.- Density profiles from the cone.

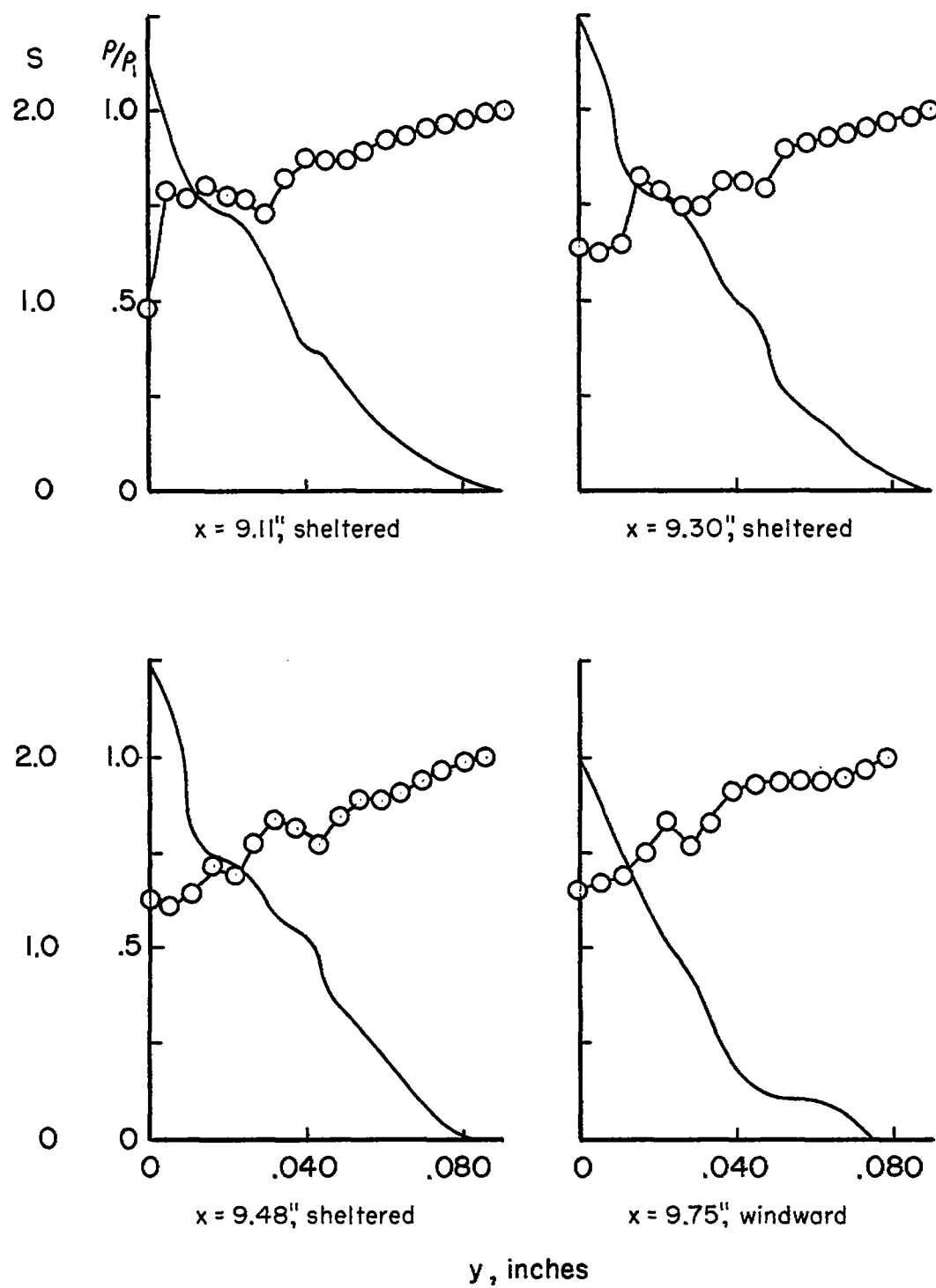


Figure 11.- Continued.

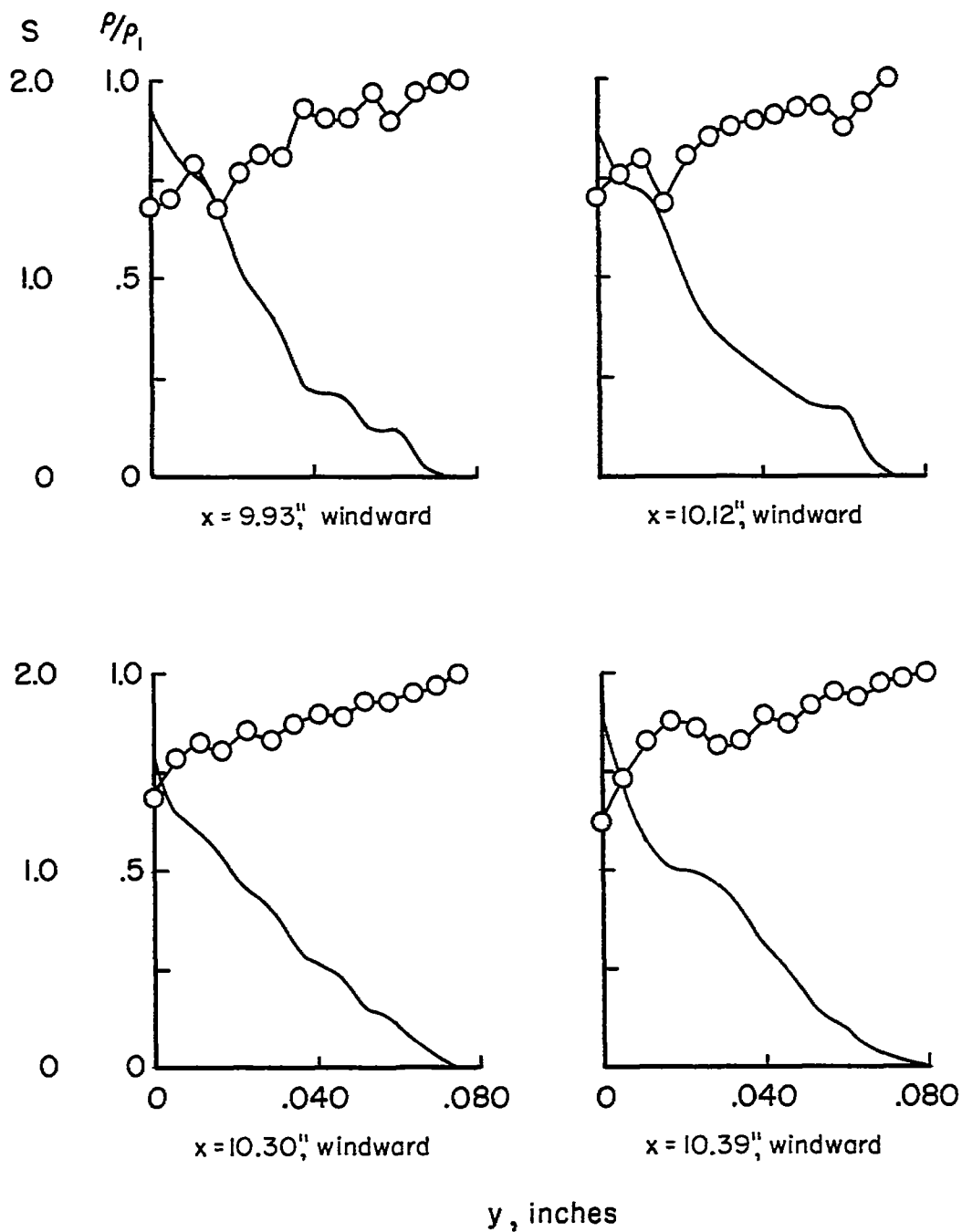
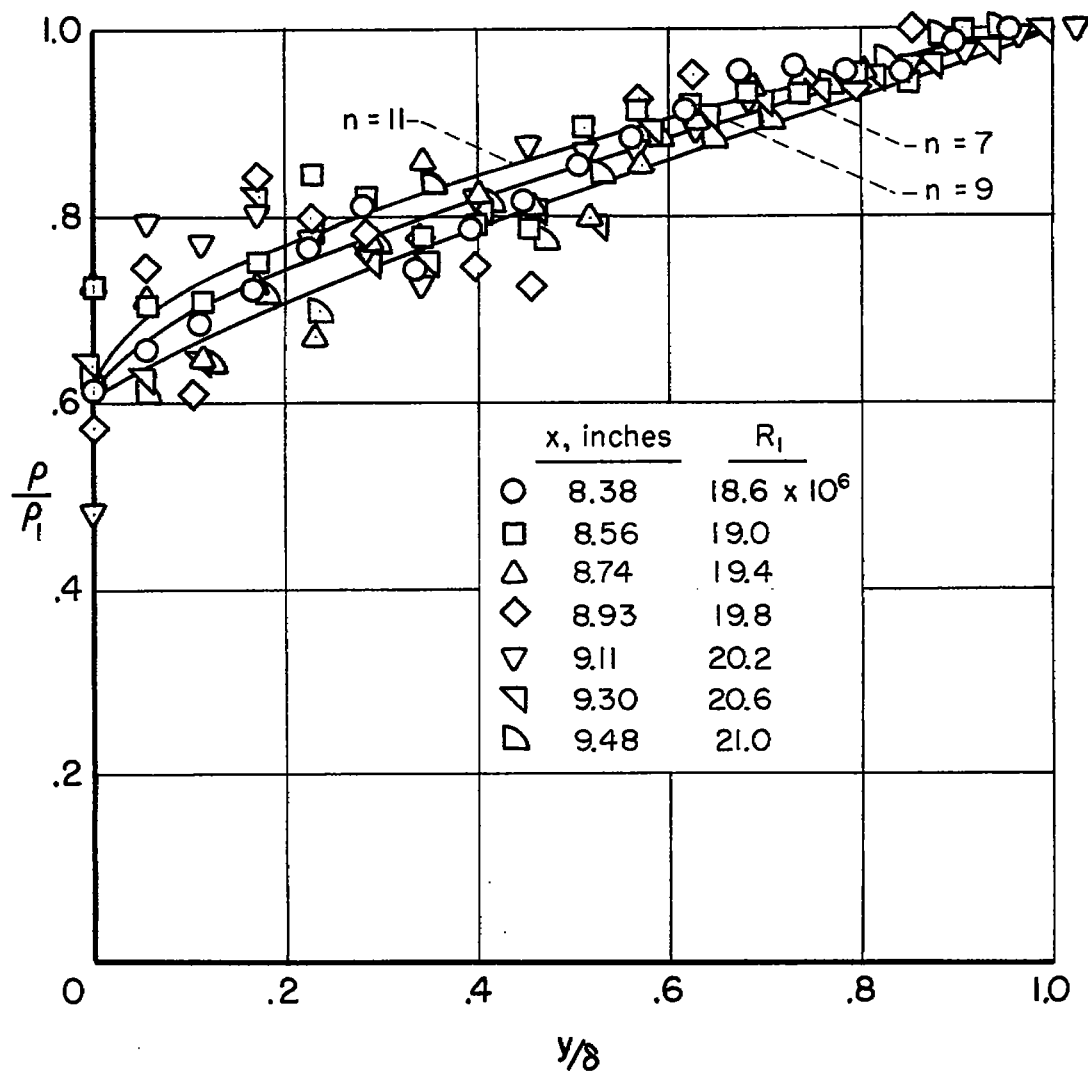
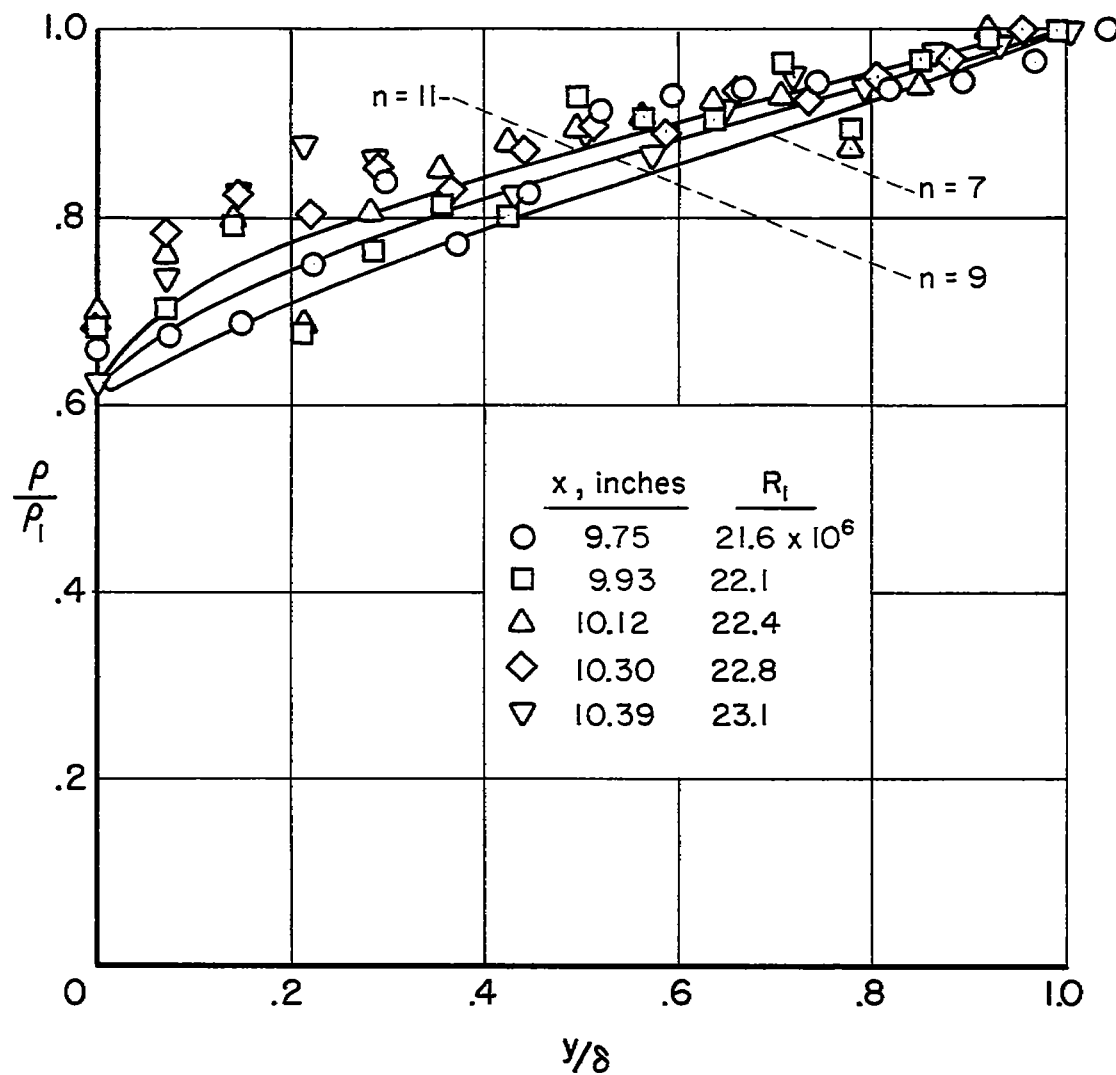


Figure 11. - Concluded.



(a) Sheltered side.

Figure 12.- Comparison of density profiles from the cone with the Crocco equation.



(b) Windward side.

Figure 12.- Concluded.

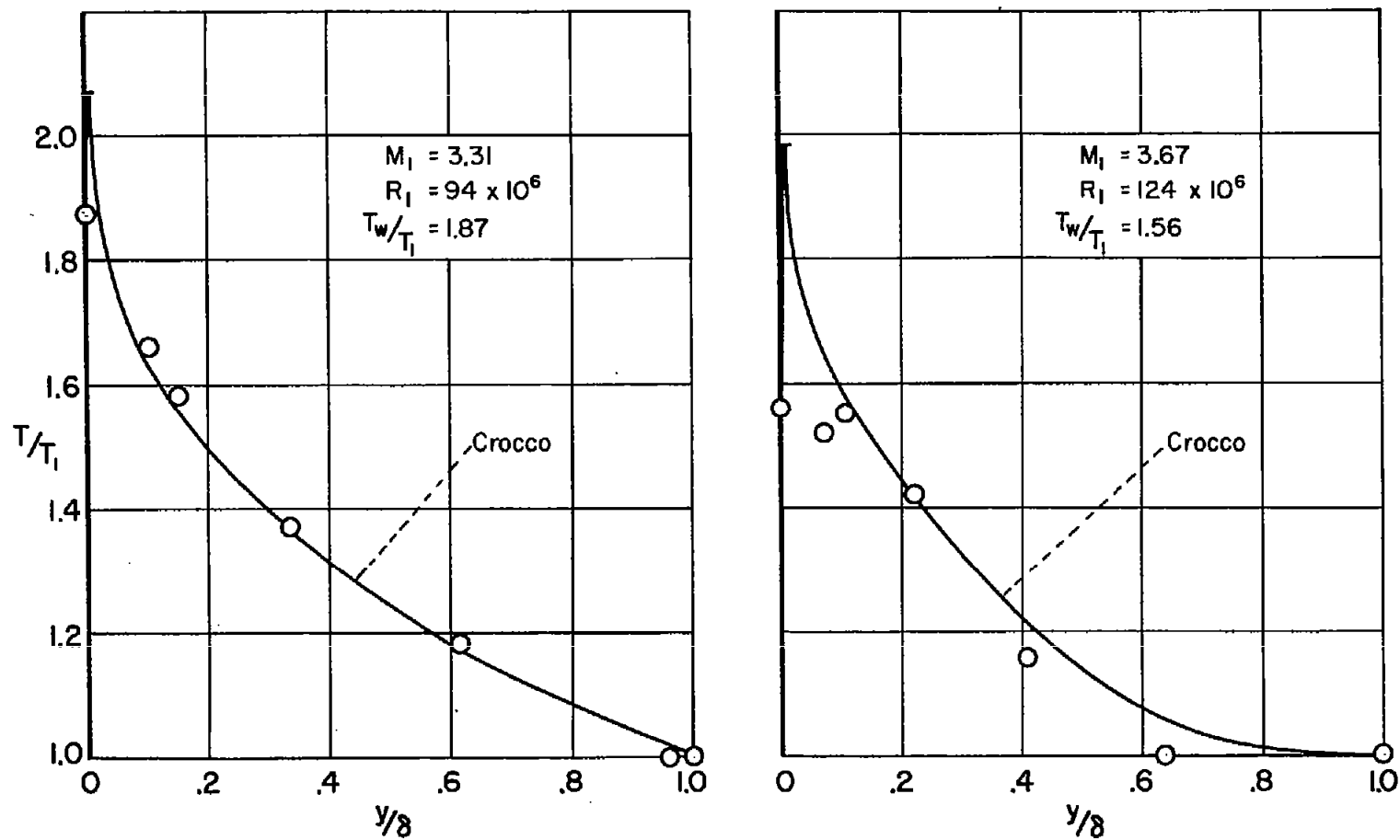


Figure 13.- Data of Swanson, Buglia, and Chauvin.

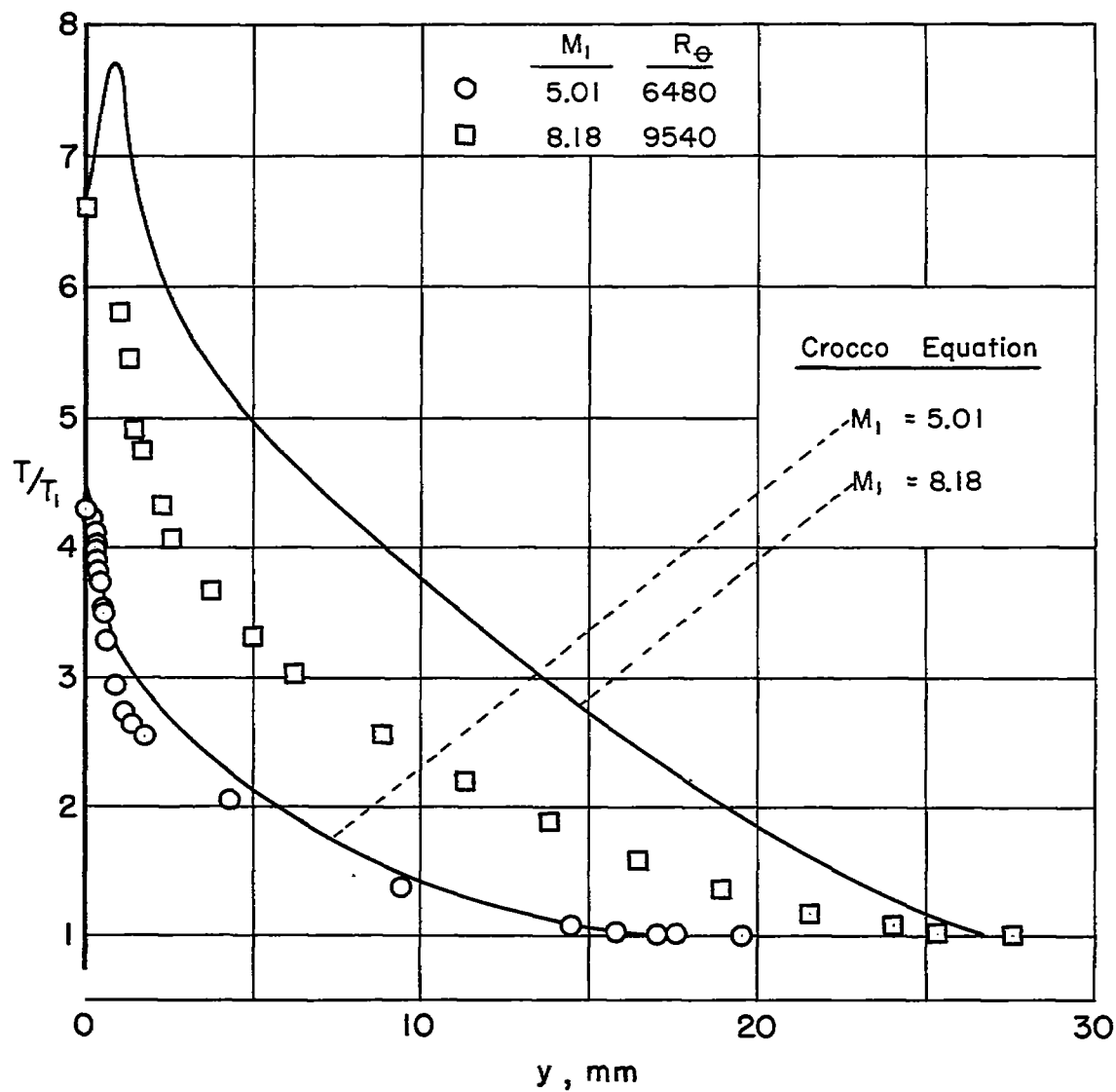


Figure 14.- Data of Lobb, Winkler, and Persh.

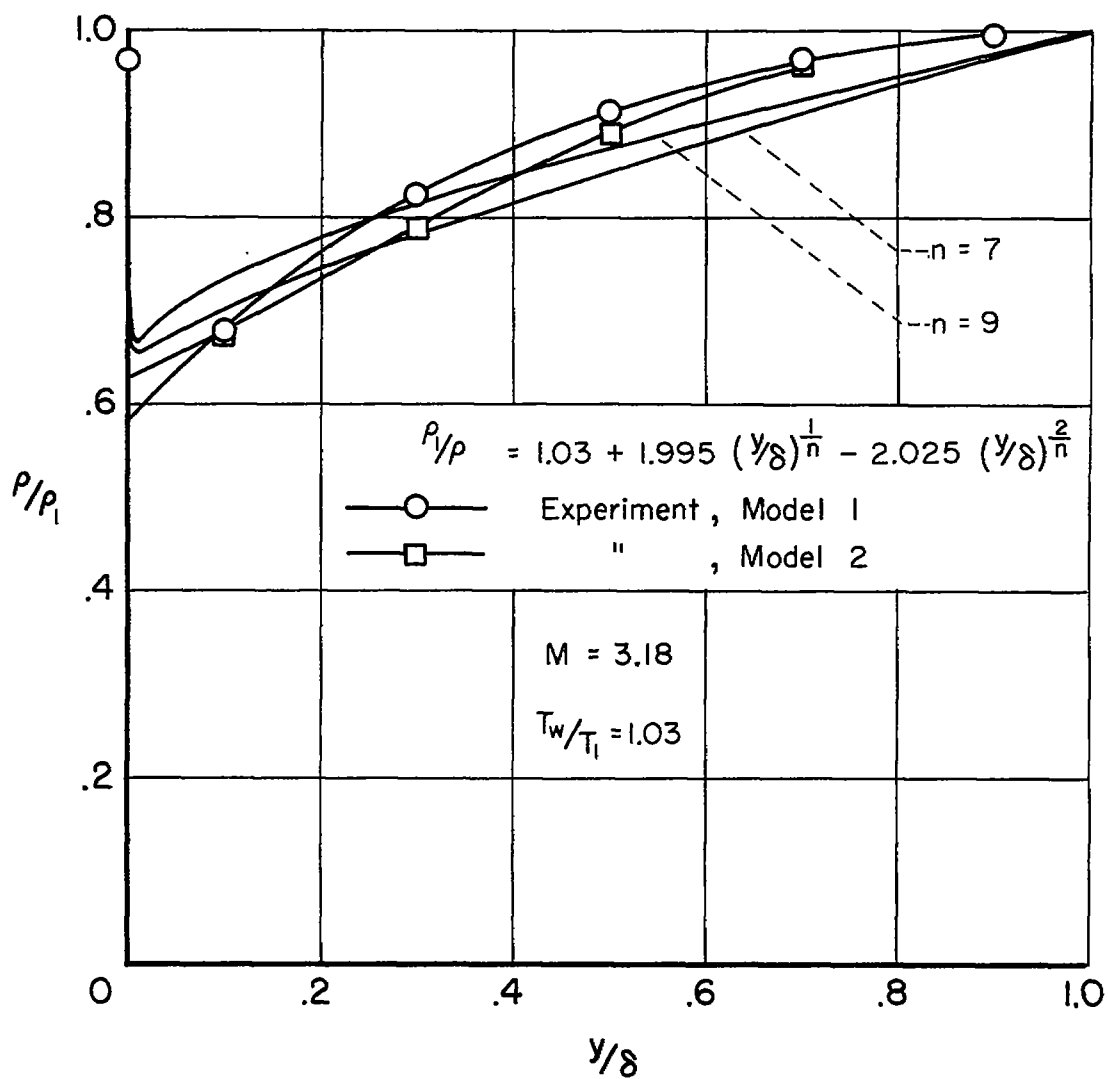


Figure 15.- Comparison of density profiles from ogive-cylinders with Crocco equation.

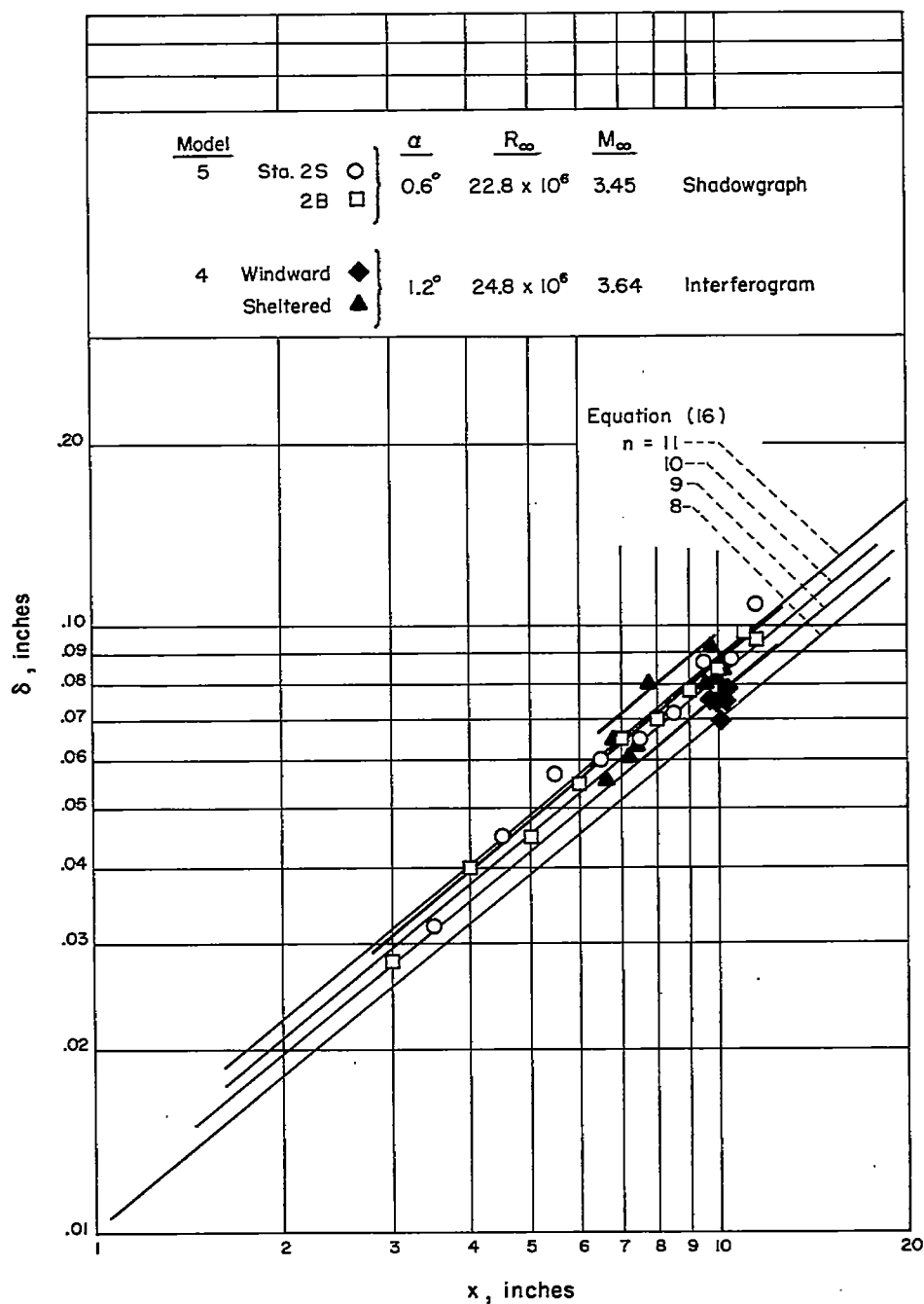
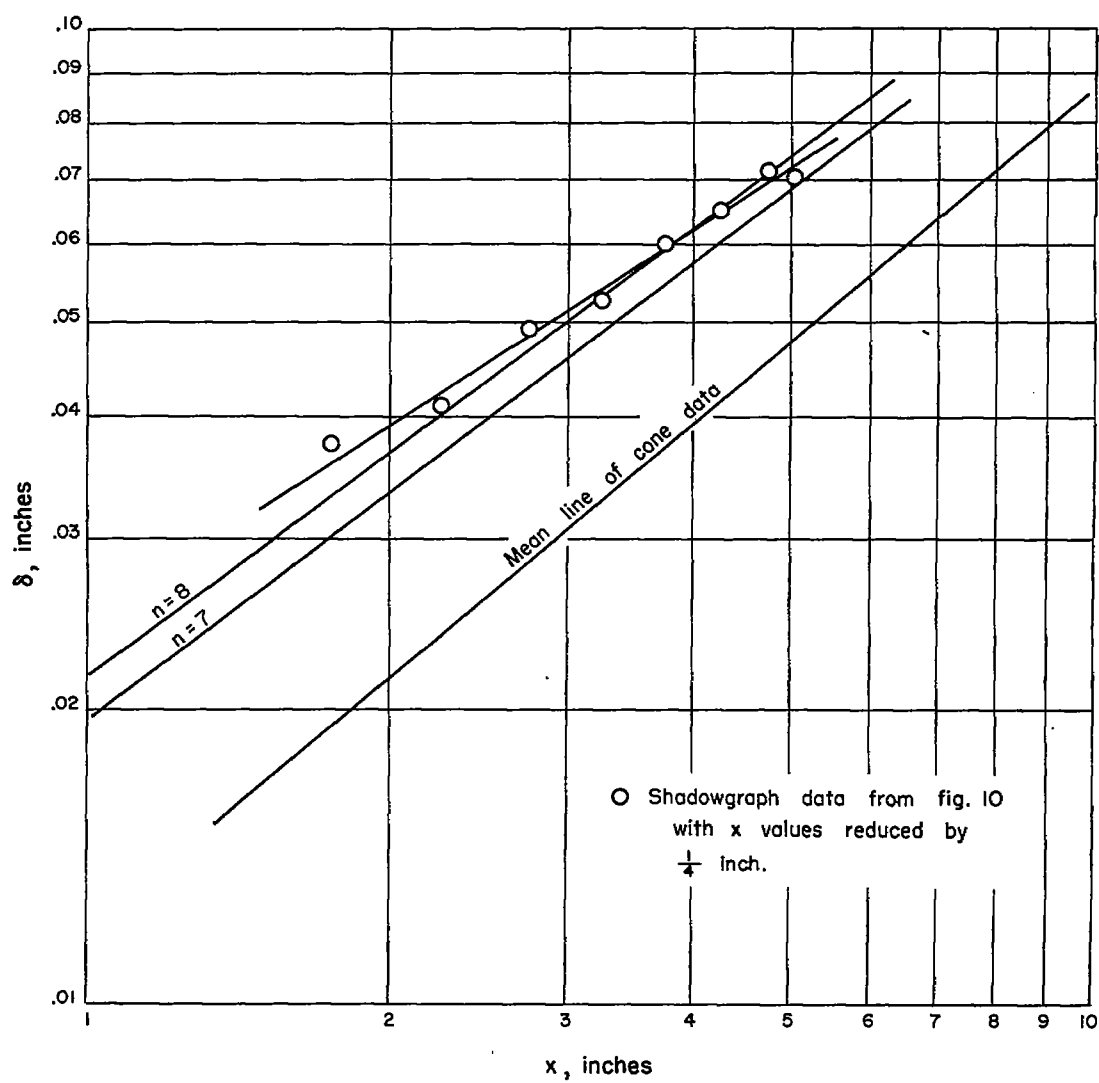


Figure 16.- Comparison of experimental and theoretical boundary-layer thicknesses.



(b) Ogive-cylinder.

Figure 16.- Concluded.

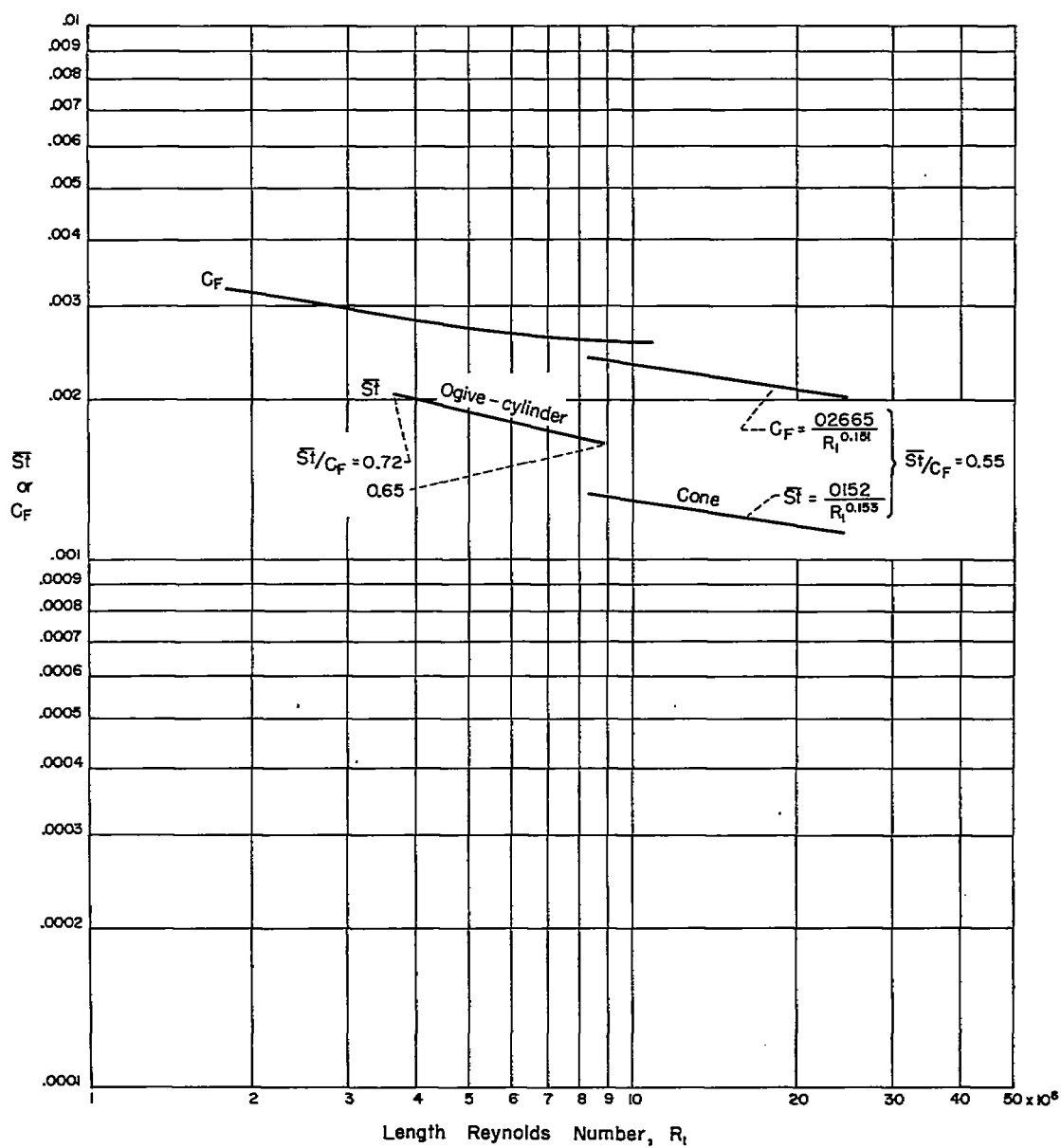
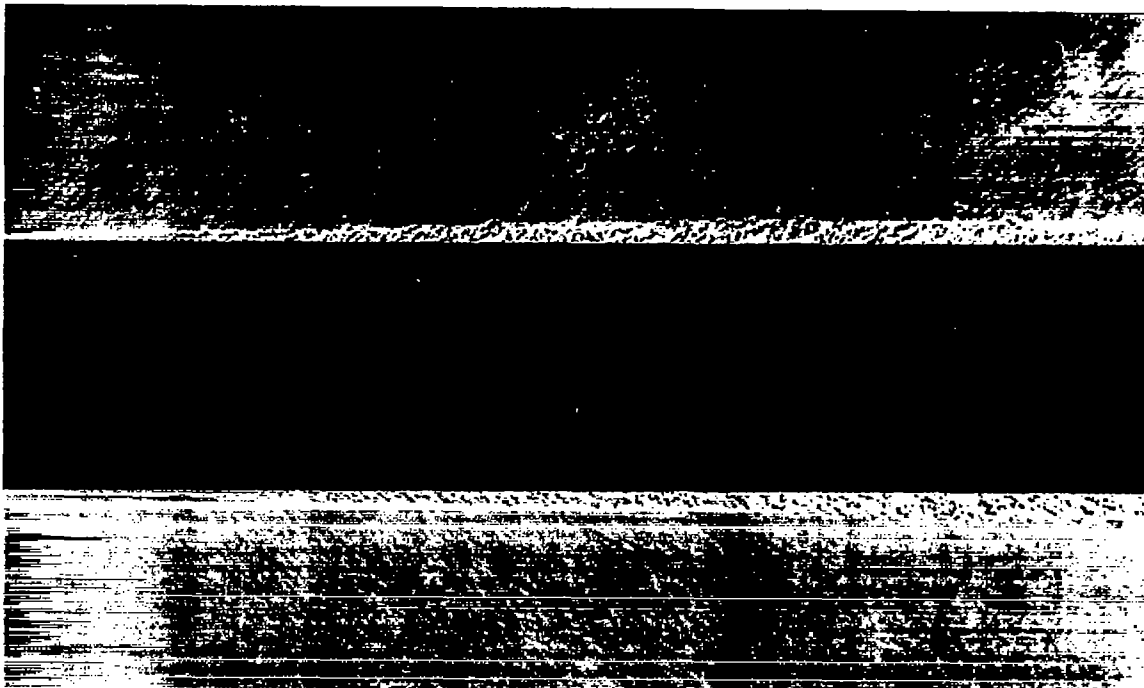
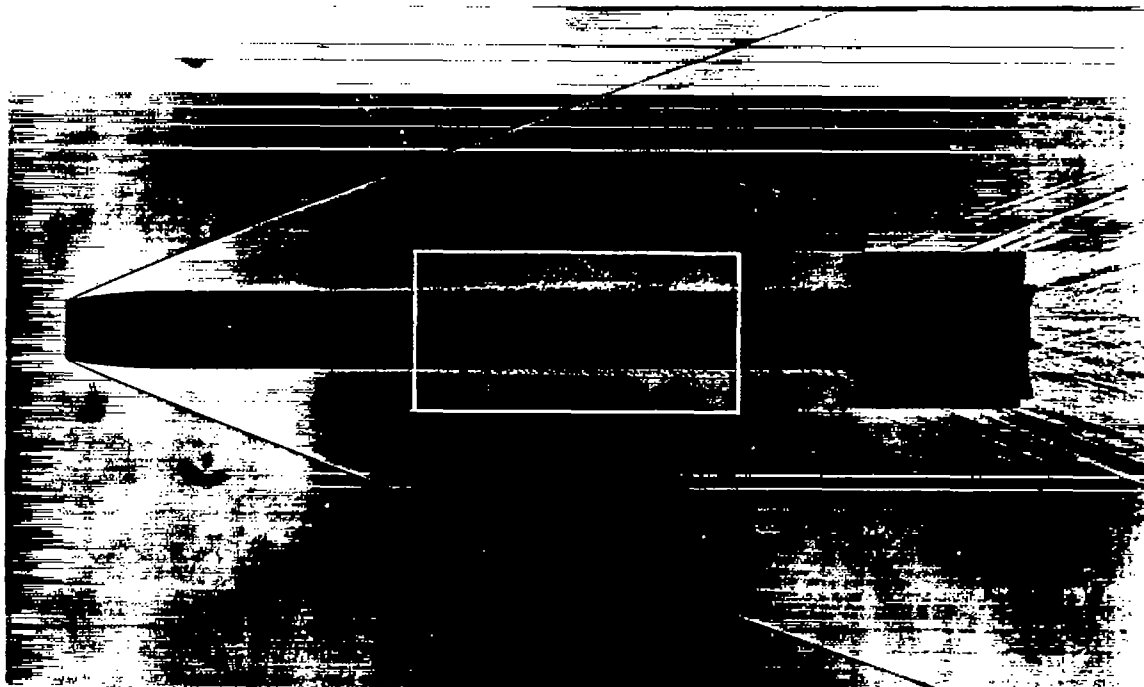


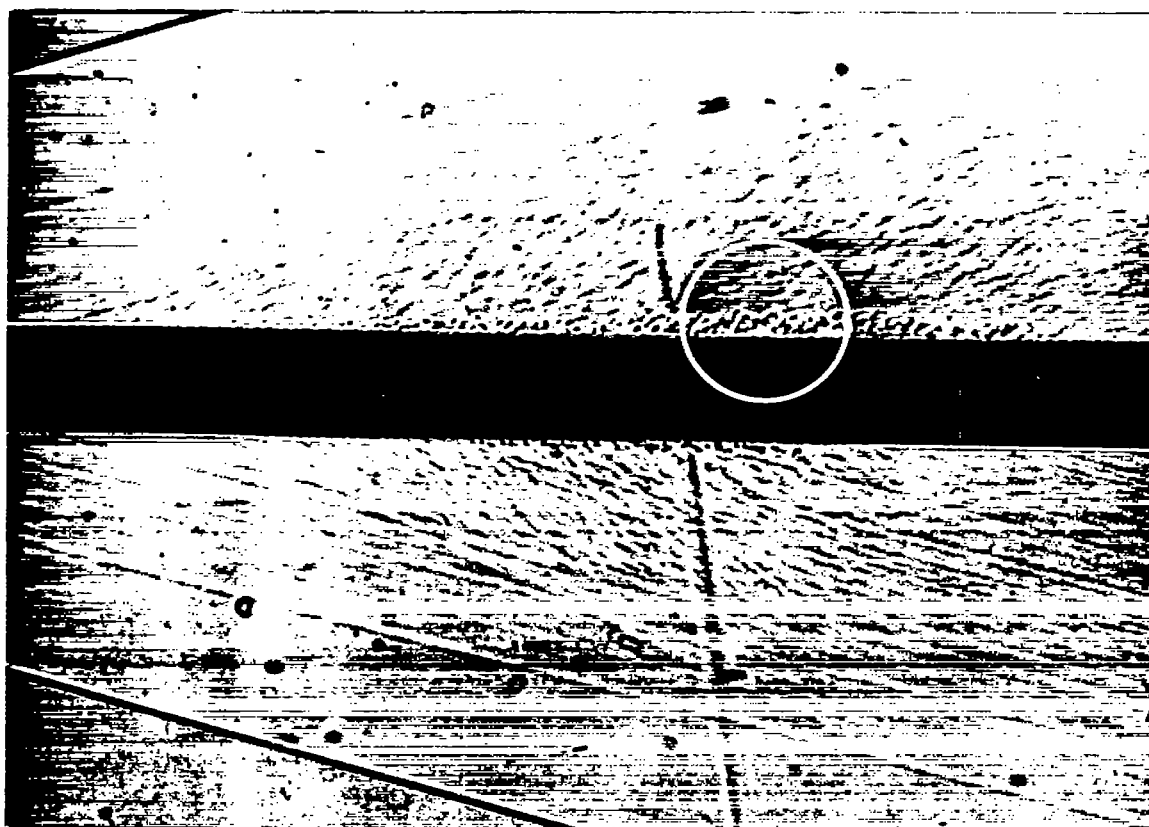
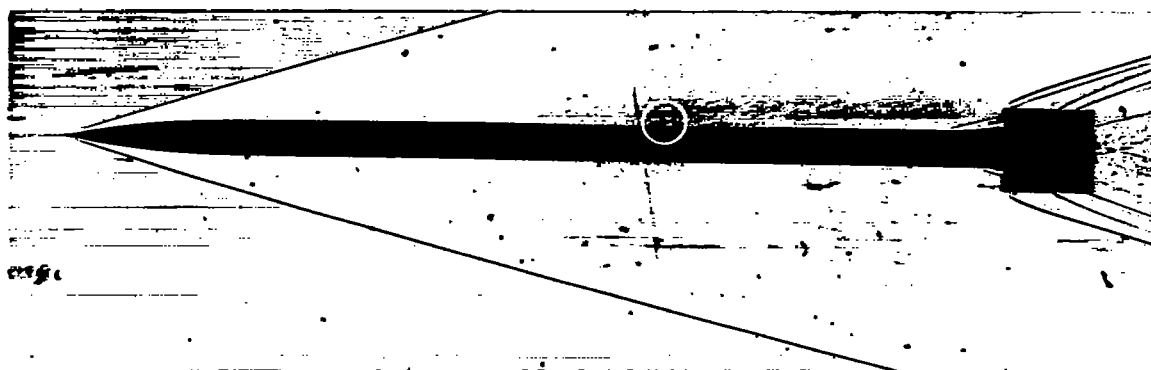
Figure 17.- Heat-transfer curves computed from experiment compared with C_f computed by T' method.



A-23779

(a) Turbulent boundary layer at an advanced stage of development.

Figure 18.- Shadowgraphs showing detailed structure of turbulent boundary layers.



(b) Turbulence in a burst, showing spots with bright centers.

A-23780

Figure 18.- Concluded.